JM PAPERS

Dynamics of nonlinear air-blown waves on falling viscous liquid films

Yanghan Meng[1], Demetrios T. Papageorgiou[1] (ORCID) and Jean-Marc Vanden-Broeck[2]

[1]Department of Mathematics, Imperial College London, London SW7 2AZ, UK

[2]Department of Mathematics, University College London, London WC1E 6BT, UK

Corresponding author: Demetrios T. Papageorgiou, d.papageorgiou@imperial.ac.uk

The dynamics of thin viscous liquid films flowing down an inclined wall under gravity in the presence of an upward flowing high-speed air stream is considered. The air stream induces nonlinear waves on the interface and asymptotic solutions are developed to derive a non-local evolution equation forced by the air pressure which is obtained analytically, and incorporating a constant tangential stress. Benney equations in the capillary (strong surface tension) and inertio-capillary regimes are derived and studied. The air stream produces Turing-type short wave instabilities in sub-critical Reynolds number regimes that would be stable in the absence of the outer flow. Extensive numerical experiments are carried out to elucidate the rich dynamics in the above-mentioned short-wave regime. The stability of different branches of solutions of non-uniform steady states is carried out, along with time-dependent nonlinear computations that are used to track the large-time behaviour of attractors. A fairly complete picture of different solution types are categorised in parameter space. The effect of the Reynolds number on the wave characteristics in the inertio-capillary regime is also investigated. It is observed that, for each value of the slenderness parameter δ, there exists a critical Reynolds number R_c above which the solutions become unbounded by encountering finite-time singularities. Increasing the air speed significantly decreases R_c, making the system more prone to large amplitude singular events even at low Reynolds numbers when the system would have been stable in the absence of the air stream.

Key words: interfacial flows (free surface), thin films, shallow water flows

1. Introduction

Falling liquid film flows have been the subject of numerous linear and nonlinear stability investigations. Gas-sheared liquid film flows arise in a number of natural phenomena

and technological applications, e.g. cooling of electronic devices, mass transfer in distillation columns and falling film flows in nuclear fusion reactors. A series of interesting hydrodynamic phenomena have been observed in gas-sheared film flows, for example, the so-called flooding event, which is a fundamental in process engineering (Semyonov 1944). A fundamental theoretical understanding of such phenomena is critical in efforts to establish dominant physical mechanisms and utilise them to investigate possible control of liquid films in diverse engineering applications.

The initiation of waves on falling liquid films sheared by a high-speed gas flow (in many cases turbulent), was initially investigated by Jeffreys (1925) a hundred years ago, who presented a linear theory using integral momentum balances to investigate the formation of roll waves. Hanratty & Hershman (1961) extended that theory and explained the initiation of roll waves by calculating the neutral stability curve. Chang (1986) derived a long-wave model that included the air effect, and the long wave stability was compared with that of Smith (1970) based on the Orr–Sommerfeld equation. With the linear stability analysis of the sheared channel flows and falling films, McCready & Chang (1996) revealed the different mechanism of the formation of large secondary disturbances or solitary waves. In the former case, the lower-frequency unstable mode was resonant with the most unstable mode, eventually leading to the formation of solitary waves of a special frequency. Alekseenko *et al.* (2009) focused on the primary instability of gas/liquid flows, and they experimentally obtained the dispersion characteristics by exciting linear waves in a wide range of frequencies. The secondary instabilities were studied by Lavalle *et al.* (2020) when the liquid film and gas flow have a comparable thickness. At high gas velocities, the secondary instability leads to flooding, while for low gas velocities the instability introduces high-frequency modulation of the wave amplitude.

The formation and dynamics of nonlinear waves on the free surface of gas-sheared film flows have also received substantial attention. Hanratty & Engen (1957) mapped out the wave transitions as the gas flow rate increases: the initially smooth liquid surface successively gave way to two-dimensional waves, squalls, roll waves and dispersed flows. Peng, Jurman & McCready (1991) found that the solitary waves on gas–liquid shear layers appeared as a secondary transition from existing large amplitude waves at low fluid Reynolds numbers. The effect of the gas velocity and liquid Reynolds number on the shape, amplitude and velocity of travelling waves were also investigated in detail (Trifonov 2010*b*; Tseluiko & Kalliadasis 2011; Kofman, Mergui & Ruyer-Quil 2017). It is also noted that the channel wall geometry also influences the patterns and dynamics of the nonlinear waves on the gas–liquid interface. Frank (2008) studied the long two-dimensional travelling waves in a channel with two different aspect ratios. It was shown that decreasing the aspect ratio suppresses the wave amplitude but increases the phase speed. Trifonov (2011) considered the influence of substrate corrugation on liquid film flowing on vertical plates as the gas velocity changes. Waves formed on the liquid–air interface and the flooding phenomenon (this is detrimental to efficient process operation) was found as the gas flow rate increased; this was characterised by the sudden increase of wave amplitude and flow reversal. Research was conducted to understand the mechanism of this event from both experimental and numerical viewpoints. Kofman *et al.* (2017) conducted various experiments and found two distinct flooding scenarios. The first is the onset of upward-moving ripples caused by a short-wave instability mode Miesen & Boersma (1995), while another scenario is the occurrence of 'slug' at high liquid Reynolds numbers. The upward-travelling ripples were also observed in Özgen *et al.* (2002) and Ishimura *et al.* (2023). Trifonov (2010*a*,*b*) investigated the onset of flooding based on

the Navier–Stokes equations and found a region of the gas velocity where two solutions exist at the same parameters and flooding takes place. The flooding points depend on the gas/liquid properties, liquid Reynolds numbers and the distance between the plates were also studied.

For modelling the perturbations of shear stress and pressure introduced by the gas flow, the Benjamin–Miles quasi-laminarity assumption is widely used (Demekhin 1981; Trifonov 2010b; Tseluiko & Kalliadasis 2011; Tsvelodub & Bacharov 2018, 2020 and references therein). In this paper, we assume that the tangential stress is constant with a known drag coefficient C_D while the pressure is determined analytically by wavy liquid films whose amplitude is small relative to the vertical extent of the outer gas region. Our approach is different from that of the recent study of Ishimura *et al.* (2023), who use the long-wave analysis in the gas region initiated by Camassa, Ogrosky & Olander (2017). We assume that the vertical extend of the gas region is large compared with the mean film thickness but of the same order as the long wavelength of the perturbations. This leads to a non-local coupling, as detailed in Tuck (1975) and King, Tuck & Vanden-Broeck (1993), with the outer inviscid gas exerting a pressure (found analytically) on the interface to drive the viscous film motion. We start from the Navier–Stokes equations in the liquid film and use asymptotic expansions in the small parameter ϵ that denotes the ratio of the mean film thickness to its wavelength, to derive two canonical evolution equations of the Benney type for the flow. First, a strong surface tension (inertialess) model, and second, an inertio-capillary model relevant at smaller values of the surface. The inertialess model is identical, after re-scaling and dropping of unsteady terms) to the equation studied in Meng, Papageorgiou & Vanden-Broeck (2024) where rich bifurcation diagrams of steady gravity–capillary air-blown waves were computed for a wide range of parameters. However, the stability of the steady solutions has not been studied and the present study undertakes this along with an extensive exploration of the nonlinear dynamics that is investigated for the first time. We also carry out extensive computations in the inertio-capillary regime and evaluate the effect of the Reynolds number and the air flow velocity on wave characteristics. In both cases the models support secondary instabilities that lead to time-periodic travelling wave solutions; such time-periodic solutions were observed in the experiments of Lavalle *et al.* (2020). The inertial Benney equation produces travelling waves that can become unbounded in finite time as parameters vary. Such singular events lead to breakdown of the equations, and we also consider the effect of the air speed on their occurrence through numerical experiments; it is shown that as the air speed increases the critical Reynolds number above which blow up occurs, decreases monotonically. There are other modelling approaches to the Benney formalism described above. These are motivated by the construction of models that can better capture linear stability features as well as the possibility of removing finite-time blow up. The reader is referred to the work of Ruyer-Quil & Manneville (2000), and references therein, that carries out improved modelling of falling film problems.

The structure of the paper is as follows. Section 2 presents the mathematical problem and describes the asymptotic analysis that leads to the strong surface tension and inertio-capillary evolution equations. Section 3 describes our numerical algorithms and includes their validation with other work. Section 4 is concerned with the strong surface tension case and presents results on the stability of steady states studied by the authors elsewhere (Meng *et al.* 2024), in addition to solving the initial value problem to map and categorising the most attracting solutions. Section 5 describes the dynamics in the inertio-capillary regime and investigates in detail the boundary in parameter space that separates travelling waves and solutions that blow up. Finally, we summarise our findings in § 6.
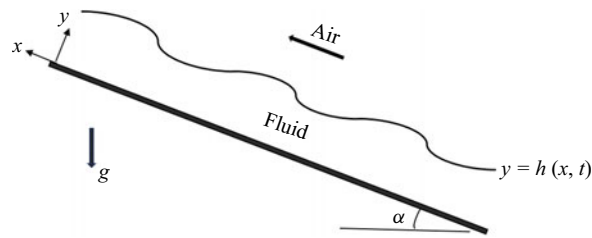
Figure 1. Schematic of the problem and coordinate system.

2. Mathematical model and derivation of the wind-driven equations

Consider a Newtonian fluid with constant density ρ_l and viscosity μ_l, flowing under gravity along a flat substrate inclined to the horizontal direction at an angle α. A schematic is given in figure 1. A Cartesian coordinate system (x, y) is introduced, where the x-axis points up the substrate and y is perpendicular to it with $y = 0$ on the substrate. The velocity in the liquid film is $\boldsymbol{u} = (u, v)$. The air–liquid surface tension coefficient is σ and the acceleration due to gravity is denoted by g. The liquid film is driven by an air stream of density ρ_a and velocity $\boldsymbol{u} = (u_a, 0)$ as $y \to \infty$. Solving the full equations of this air/liquid flow is a challenging direct numerical simulation problem. We are interested in exploiting the multi-scale nature of the problem in the presence of the air stream found in applications, and in what follows we make certain assumptions to derive reduced dimension systems that allow us to study extensively the nonlinear dynamics. The analysis leading to the evolution equations studied here follows and extends the work of King *et al.* (1993) by incorporating inertia effects.

We begin with the dimensional problem. The flow in the viscous liquid film is governed by the Navier–Stokes equations

$$\rho \left(\boldsymbol{u}_t + (\boldsymbol{u} \cdot \boldsymbol{\nabla})\boldsymbol{u}) \right) = -\boldsymbol{\nabla} p + \mu_l \nabla^2 \boldsymbol{u} - \rho_l g (\sin \alpha, \cos \alpha), \tag{2.1}$$

$$\boldsymbol{\nabla} \cdot \boldsymbol{u} = 0, \tag{2.2}$$

subject to no slip at the wall (p is the pressure)

$$u = v = 0, \qquad \text{at} \quad y = 0, \tag{2.3}$$

a kinematic boundary condition at the free surface

$$v = h_t + u h_x, \qquad \text{at} \quad y = h(x, t), \tag{2.4}$$

along with normal and tangential stress balances at the interface $y = h(x, t)$

$$\frac{1}{(1 + h_x^2)} \left(4\mu_l h_x v_y + \mu_l (1 - h_x^2)(u_y + v_x) \right) = \tau_s, \tag{2.5}$$

$$p_A - p + 2\mu_l \frac{1 + h_x^2}{1 - h_x^2} v_y = \frac{\sigma h_{xx}}{(1 + h_x^2)^{3/2}}. \tag{2.6}$$

One of our modelling assumptions is that $\tau_s = (1/2)\rho_a u_a^2 C_D$ in (2.5) is a constant that represents the shear exerted by the outer flow on the liquid film (C_D is the constant drag coefficient). The effect of non-uniform tangential stress will be discussed in detail later. In (2.6) p_A represents the pressure just above the interface exerted by the air flow accounting for coupling between the two phases. The airflow is assumed to be inviscid, incompressible and irrotational. Introducing a velocity potential ϕ so that $\boldsymbol{u} = \boldsymbol{\nabla}\phi$ in the

air region, and considering two-dimensional flows we have

$$\phi_{xx} + \phi_{yy} = 0, \qquad y > h(x, t). \tag{2.7}$$

At the air–liquid interface $y = h(x, t)$, we must satisfy kinematic and dynamic boundary conditions which read

$$h_t + \phi_x h_x = \phi_y, \tag{2.8}$$

$$\phi_t + \frac{1}{2}\left(\phi_x^2 + \phi_y^2\right) + \frac{p_a}{\rho_a} = \frac{1}{2}u_A^2, \tag{2.9}$$

where ρ_a is the density of the air and the Bernoulli constant $u_a^2/2$ follows from the condition at $y = \infty$.

The equations in the liquid film are the incompressible Navier–Stokes equations. Lengths in the vertical and horizontal directions are non-dimensionalised by the undisturbed liquid layer depth H and a typical wavelength λ, respectively. We assume that $\delta = H/\lambda \ll 1$ since the layer is thin. The horizontal velocity is scaled with the Nusselt scale $U_0 = (\rho_l g H^2 \sin \alpha)/2\mu_l$, the vertical velocity by δU_0 due to mass conservation, time by $t_0 = \lambda/U_0$ and the pressure by $\rho_l U_0^2$. We write $h = H\tilde{h}$, $u = U_0\tilde{u}$, $v = \delta U_0\tilde{v}$, $t = t_0\tilde{t}$ and $p = \rho_l U_0^2 \tilde{p}$, substitute into (2.1), (2.2) and boundary conditions (2.3)–(2.6) and drop tildes to find

$$\delta\left(u_t + uu_x + vu_y\right) = -\delta p_x + \frac{1}{R}\left(\delta^2 u_{xx} + u_{yy}\right) - \frac{2}{R}, \tag{2.10}$$

$$\delta^2\left(v_t + uv_x + vv_y\right) = -p_y + \frac{1}{R}\left(\delta^3 v_{xx} + \delta v_{yy}\right) - \frac{2}{R}\cot\alpha, \tag{2.11}$$

$$u_x + v_y = 0, \tag{2.12}$$

subject to

$$u = v = 0, \qquad \text{at} \quad y = 0, \tag{2.13}$$

$$v = h_t + uh_x, \qquad \text{at} \quad y = h, \tag{2.14}$$

$$4\delta^2 h_x v_y + \left(1 - \delta^2 h_x^2\right)\left(u_y + \delta^2 v_x\right) = CC_D\left(1 + \delta^2 h_x^2\right), \qquad \text{at} \quad y = h, \tag{2.15}$$

$$CP_a - \frac{1}{2}Rp + \delta\frac{1 + h_x^2}{1 - h_x^2}v_y = \frac{\delta^2 h_{xx}}{2D(1 + \delta^2 h_x^2)^{3/2}}, \qquad \text{at} \quad y = h, \tag{2.16}$$

where we have used the outer pressure scaling $p_a = \rho_a u_a^2 P_a$. The dimensionless parameters appearing above are a Reynolds number R, an air-speed parameter C and a capillary number D

$$R = \frac{\rho_l U_0 H}{\mu_l} = \frac{\rho_l^2 g H^3 \sin\alpha}{2\mu_l^2}, \quad C = \frac{\frac{1}{2}\rho_a u_a^2 H}{\mu_l U_0} = \frac{\rho_a u_a^2}{\rho_l g H \sin\alpha}, \quad D = \frac{\mu_l U_0}{\sigma} = \frac{\rho_l g H^2 \sin\alpha}{2\sigma}. \tag{2.17}$$

As mentioned above, in our model the coupling between the air stream and the liquid film is through the dimensionless air pressure term $p_a/\rho g H \sin\alpha$ in the normal stress balance (2.16). Before analysing the liquid film flow we derive an expression for this pressure that is in terms of the interfacial position $h(x, t)$, thus producing a single evolution equation for $h(x, t)$ as we show subsequently.

Next we consider the dimensionless form of the outer problem given by (2.7) and boundary conditions (2.8)–(2.9). Observing that the air region is thick relative to the liquid layer thickness (expected in applications), we introduce a new variable $Y = O(1)$ given by

$y = \lambda Y$ (recall that $x = \lambda \tilde{x}$ with tildes dropped). Velocities scale with u_a and hence we write $\phi = u_a \lambda \Phi$, which casts (2.7) into its dimensionless form

$$\Phi_{xx} + \Phi_{YY} = 0, \qquad Y > \delta h(x, t). \tag{2.18}$$

To non-dimensionalise (2.8)–(2.9) we write $p_a = \rho_a u_a^2 P_a$ (as in (2.16)) and use the time scale t_0 introduced earlier to find

$$\frac{\delta U_0}{u_a} h_t + \delta \Phi_x h_x = \Phi_Y, \qquad \text{on} \quad Y = \delta h(x, t), \tag{2.19}$$

$$\frac{U_0}{u_a} \Phi_t + \frac{1}{2}\left(\Phi_x^2 + \Phi_Y^2\right) + P_a = \frac{1}{2}, \qquad \text{on} \quad Y = \delta h(x, t). \tag{2.20}$$

An asymptotic solution to (2.18)–(2.20) can be found as follows:

$$\Phi = x + \delta \Phi_1 + \cdots, \qquad P_a = \delta P_{a0} + \cdots. \tag{2.21}$$

The leading-order problem is

$$\Phi_{1xx} + \Phi_{1YY} = 0, \qquad Y > 0, \tag{2.22}$$

subject to

$$h_x = \Phi_{1Y}, \qquad \text{on} \quad Y = 0, \tag{2.23}$$

$$\Phi_{1x} + P_{a0} = 0, \qquad \text{on} \quad Y = 0, \tag{2.24}$$

where in arriving at (2.24) we have assumed that $U_0/u_a \ll 1$ and the outer problem is quasi-steady to leading order. For a physical example of an oil film having millimetric thickness on an incline with angle $\alpha = \pi/6$, we have $U_0 \approx 5 \times 10^{-3}$ m s^{-1}, and hence if the outer flow has speed $u_a = 10$ m s^{-1} (i.e. 36 km h^{-1}) then we find $U_0/u_a < 10^{-3}$. The problem (2.22)–(2.24) can be solved in different ways (e.g. Fourier transforms or equivalently complex variable formulation and Cauchy's theorem) to give the perturbation pressure in the air that couples into the normal stress balance (2.16). The result is

$$P_{a0} = -\mathcal{H}[h_x], \qquad \mathcal{H}[g](x) = \frac{1}{\pi} \int_{-\infty}^{\infty} \frac{g(\xi)\,\mathrm{d}\xi}{x - \xi}, \tag{2.25}$$

and $\mathcal{H}$ is the Hilbert transform operator. The result above provides an explicit dependence of P_{a0} on $h(x, t)$ and hence the liquid film problem can be addressed as a closed system. We do this next in two scenarios, an inertialess and an inertial one.

2.1. *Surface tension dominated regime*

Inspection of the normal stress balance condition (2.16) shows that a small capillary number $D = \delta^3 \overline{D}$ (here and in what follows bars denote order one quantities) induces a pressure in the film of order $1/\delta$. To retain the external flow effects and recalling the expansion (2.21), we conclude that $C = \delta^{-2} \overline{C}$. The large capillary pressure drives an order one flow in the film and the appropriate expansions are $u = u_0 + O(\delta)$, $v = v_0 + O(\delta)$, $p = \delta^{-1} p_0 + O(1)$, $h = h_0 + O(\delta)$. To retain gravitational effects we need small inclination angles $\alpha = O(\delta)$ and write $\cot \alpha = G/\delta$ where G is a constant. Substitution into (2.10)–(2.12) gives

$$-p_{0x} + \frac{1}{R} u_{0yy} - \frac{2}{R} = 0, \tag{2.26}$$

$$p_{0y} + \frac{2}{R} G = 0, \tag{2.27}$$

$$u_{0x} + v_{0y} = 0. \tag{2.28}$$

The no-slip conditions (2.13), (2.14) are unchanged besides dependent variables gaining a subscript 0. To retain shear stresses in (2.15) we need $CC_D = O(1)$ since the left-hand side is of $O(1)$. Hence, we write $CC_D = \overline{\tau}$ with $\overline{\tau}$ an order one constant. The kinematic condition (2.14) and the stress balances (2.15)–(2.16) give to leading order

$$v_0 = h_{0t} + u_0 h_{0x}, \quad \text{at} \quad y = h_0, \tag{2.29}$$

$$u_{0y} = \overline{\tau}, \quad \text{at} \quad y = h_0, \tag{2.30}$$

$$-\overline{C}\mathcal{H}[h_{0x}] - \frac{1}{2}R p_0 = \frac{1}{2\overline{D}}h_{0xx}, \quad \text{at} \quad y = h_0, \tag{2.31}$$

where the solution (2.25) has been used. A single equation for $h_0(x, t)$ is obtained as follows. Integration of (2.27) gives $p_0 = \overline{p}_0(x, t) - 2Gy/R$, while integration of (2.26) with respect to y, use of no slip $u_0(x, 0, t) = 0$ and the tangential stress balance (2.30) gives $u_0 = y(y - 2h_0)[(1/2)R\overline{p}_{0x} + 1] + \overline{\tau}h_0$. Mass conservation (2.28) immediately yields v_0 after the condition $v_0(x, 0, t) = 0$ is used. The normal stress balance (2.31) gives $R\overline{p}_0 = -2\overline{C}\mathcal{H}[h_{0x}] + 2Gh_0 - (1/\overline{D})h_{0xx}$. Using this in the solutions for u_0 and v_0 and substituting the velocities into (2.29) provides the desired evolution equation

$$h_{0t} + \left[-\frac{2h_0^3}{3} + \frac{\overline{\tau}}{2}h_0^2 - \frac{2G}{3}h_0^3 h_{0x} + \frac{\overline{2C}}{3}\mathcal{H}[h_{0xx}]h_0^3 + \frac{1}{3\overline{D}}h_{0xxx}h_0^3 \right]_x = 0. \tag{2.32}$$

Equation (2.32) is solved on periodic domains of dimensionless size L, i.e. $h(x, t) = h(x + L, t)$. The size L is a crucial dimensionless parameter with the number of linearly unstable modes increasing with L. In order to compare with the results of Meng *et al.* (2024) we rescale to spatial domains of unit length. This is achieved by writing $x = L\overline{x}$, $h = (\overline{\tau}/2)\overline{h}$, and $t = (12L/\overline{\tau}^2)\overline{t}$, to cast (2.32) into (after dropping bars)

$$h_t + 2\left[\left(\frac{v^2 \pi}{d_1}\mathcal{H}[h_{xx}] + \frac{v^3}{d_2}h_{xxx} - v h_x - 1 \right) h^3 + \frac{3}{2}h^2 \right]_x = 0, \tag{2.33}$$

where

$$d_1 = \frac{\pi G^2 \overline{\tau}}{\overline{C}}, \qquad d_2 = \frac{\overline{D}\overline{\tau}^2 G^3}{2}, \qquad v = \frac{G\overline{\tau}}{2L}, \tag{2.34}$$

where d_1 measures the induced drag, d_2 is a scaled Bond number (small d_2 implies large surface tension) and v is inversely proportional to the size of the system (small v corresponds to large dimensionless wavelengths). Equation (2.33) is identical to the problem studied in Meng *et al.* (2024) (a factor of 2 is removable by the additional rescaling $\overline{\tau} \rightarrow 2\overline{\tau}$ which is due to a factor of 2 difference in the non-dimensionalisation of the shear stress in the present study), and is to be solved on spatially periodic domains of unit length. Version (2.33) is very useful because it enables us to directly study the stability and dynamics of the nonlinear bifurcation branches computed in Meng *et al.* (2024). This is undertaken later.

2.2. *The inertio-capillary regime*

This regime arises when the capillary number is not as small as in § 2.1 so that pressure perturbations due to surface tension and the air stream are $\mathcal{O}(1)$; this happens when $D = \delta^2 \overline{D}$ in (2.16), the angle $\cot \alpha = \mathcal{O}(1)$, $C = \delta^{-1}\overline{C}$ and R, $\overline{\tau}$ being order one constants. The leading-order pressure P_{a0} in the air region is given by (2.25). Expanding variables in the liquid film, $u = u_0 + \delta u_1 + \cdots$, $v = v_0 + \delta v_1 + \cdots$, $p = p_0 + \delta p_1 + \cdots$, $h = h_0 +$

$\delta h_1 + \cdots$ and substituting into (2.10)–(2.12) gives to leading order

$$u_{0yy} = 2, \qquad p_{0y} = -\frac{2}{R}\cot\alpha, \qquad u_{0x} + v_{0y} = 0, \tag{2.35}$$

which gives, using the no-slip and tangential shear-stress conditions

$$u_0 = y(y - 2h_0) + \overline{\tau}y, \qquad v_0 = h_{0x}y^2, \qquad p_0 = -\frac{2\cot\alpha}{R}y + \overline{p}_0(x, t). \tag{2.36}$$

The pressure $\overline{p}_0$ follows from the normal stress balance condition (2.16) at leading order

$$\frac{1}{2}R\overline{p}_0(x, t) = \cot\alpha\, h_0 - \overline{C}\mathcal{H}[h_{0x}] - \frac{1}{2\overline{D}}h_{0xx}. \tag{2.37}$$

The kinematic condition (2.14) gives, to leading order

$$h_{0t} + \left(\frac{\overline{\tau}}{2}h_0^2 - \frac{2}{3}h_0^3\right)_x = 0. \tag{2.38}$$

Similar leading-order behaviour was found in Tseluiko & Papageorgiou (2006). Solutions of (2.38) for fairly general initial conditions (e.g. smooth spatially periodic initial data) encounter infinite slopes in finite time heralding the breakdown of the long-wave asymptotic expansion. The singularity can be regularised by incorporating high-order terms including surface tension, as done by Tseluiko & Papageorgiou (2006) in a related problem. The analysis leading to the desired evolution equation (2.39) below, is provided in Appendix A

$$h_t + \left[-\frac{2}{3}h^3 + \frac{\overline{\tau}}{2}h^2 + \delta\left(\frac{8R}{15}h^6 - \frac{4R\overline{\tau}}{15}h^5 - \frac{2\cot\alpha}{3}h^3\right)h_x + \frac{2\delta\overline{C}}{3}h^3\mathcal{H}[h_{xx}]\right.$$
$$\left. + \frac{\delta}{3\overline{D}}h^3 h_{xxx}\right]_x = 0. \tag{2.39}$$

Equation (2.39) agrees with that in Tseluiko & Papageorgiou (2006) in the absence of the air stream here and no electric field in that study. Equation (2.39) is solved on L-periodic domains, i.e. $h(x, t) = h(x + L, t)$. In the computations presented in §5 we take $L = 1$ and also increase it to $L = 2\pi$ in order to evaluate the effect of domain size on the solution.

3. Numerical solution of the evolution equations

3.1. *Numerical methods and validation*

To fix matters, we will describe our numerical methods for the inertio-capillary (2.39). Totally analogous schemes are implemented to solve (2.33). Either equation is written as

$$h_t + \mathcal{A}(h) = \mathcal{B}(h), \tag{3.1}$$

where the nonlinear operator $\mathcal{A}(h)$ contains terms involving $h^3 h_{xxxx}$, $h^3\mathcal{H}[h_{xxx}]$ and $h^3 h_{xx}$, and all remaining terms are grouped into $\mathcal{B}(h)$. For (2.39) these are

$$\mathcal{A}(h) = (A_1\mathcal{H}[h_{xxx}] + A_2 h_{xxxx} - A_3 h_{xx})\, h^3, \tag{3.2}$$

$$\mathcal{B}(h) = \left[B_1 h^3 + B_2 h^2 + \delta B_3\left(\frac{8R}{15}h^6 - \frac{4R}{15}CC_D h^5\right)h_x\right]_x$$
$$+ 3h^2 h_x (A_1\mathcal{H}[h_{xx}] + A_2 h_{xxx} - A_3 h_x), \tag{3.3}$$

and analogous expressions with different coefficients A_i and B_i arise for (2.33). In our numerical schemes the function $\mathcal{A}(h)$ is treated implicitly whilst the part $\mathcal{B}(h)$ is evaluated explicitly. Spatially periodic domains $[0, L]$ are considered (all computations in the present work use $L = 1$ unless stated otherwise). On implementing the schemes, the spatial domain $[0, L]$ is split into N (odd) equidistant points and the time step is defined by dt; typically we take $dt \approx 10^{-4}$ or smaller to guarantee the conservation of the mean film thickness $\int_0^L h(x, t)dx$ as dictated by the equation. Second-order backward differentiation formulas (BDF) are used for the time discretisation (see Akrivis *et al.* (2011) for all BDF formulas up to sixth-order accuracy)

$$\frac{3}{2}h^{n+2} + dt\,\mathcal{A}(h^{n+2}) = 2h^{n+1} + 2dt\,\mathcal{B}(h^{n+1}) - \frac{1}{2}h^n - dt\,\mathcal{B}(h^n). \qquad (3.4)$$

To start the time integration (3.4), we need h^1 starting from the initial condition h^0. This is achieved by one step of the implicit Euler method. After computation of h^n and h^{n+1}, the implicit time stepping requires solution of a nonlinear system to obtain h^{n+2}. There are N unknowns, h_j^{n+2}, at the collocation points $j = 1, 2, 3 \cdots N$. Newton's method is applied to solve the resultant nonlinear algebraic systems at the collocation points. The Jacobian matrix is computed analytically prior to each iteration by taking advantage of spectral matrices. Iterations are terminated when the error is less than 10^{-8}, thus guaranteeing accurate results. The square matrix of the discrete Hilbert transform, denoted by $\mathbb{H}$, is given by

$$\mathbb{H}(i, j) = \begin{cases} \frac{1-(-1)^{i-j}}{2N} \cot\left(\frac{\pi(i-j)}{2N}\right) - \frac{1+(-1)^{i-j}}{2N} \tan\left(\frac{\pi(i-j)}{2N}\right), & \mathrm{mod}(i-j, N) \not\equiv 0 \\ 0, & \mathrm{mod}(i-j, N) \equiv 0, \end{cases}$$
$$(3.5)$$

and the first derivative matrix is given by

$$\mathbb{D}(i, j) = \begin{cases} 0, & \mathrm{mod}(i-j, 2) \equiv 0, \\ \frac{(-1)^{(i-j)}\pi}{L} \csc\left(\frac{\pi(i-j)}{N}\right), & \mathrm{mod}(i-j, 2) \not\equiv 0, \end{cases} \qquad (3.6)$$

where L is the spatial period mentioned above (see Trefethen (2000) for detailed derivations). For the inertia-less model (2.33) we take $L = 1$ and vary ν to study waves of different unscaled wavelengths, while for the inertio-capillary regime, the effect of computation domain sizes is directly examined by changing L.

To verify the numerical scheme, we perform the time integration for models with and without inertia, and numerical parameters $N = 501$ and $dt = 10^{-4}$. In the first numerical experiment, we select a small amplitude initial condition $h = 1 + 0.02\cos(2\pi x)$, so that the growth rate at an early stage can be predicted by the linear theory in Meng *et al.* (2024). Figure 2(*a*) shows the evolution of the wave amplitude (solid blue curve) superimposed with the prediction of linear theory; agreement is seen to be excellent prior to nonlinear saturation effects that enter around $t \approx 0.8$. For the second computation, we compute a steady solution of (2.39) and use it as the initial condition in our code. Figure 2(*b*) shows the time evolution and as expected the solution remains unchanged (to within truncation errors) for a relatively large computed time $t = 40$, verifying once again the accuracy of our algorithms. To classify different types of unsteady solutions as parameters vary we follow the energy $E = \int_0^1 h^2(x, t)dx$ of the solutions The maxima and minima of $E(t)$ are tracked to construct numerically Poincaré maps in order to probe the complexity of the dynamics – see for example Smyrlis & Papageorgiou (1991).
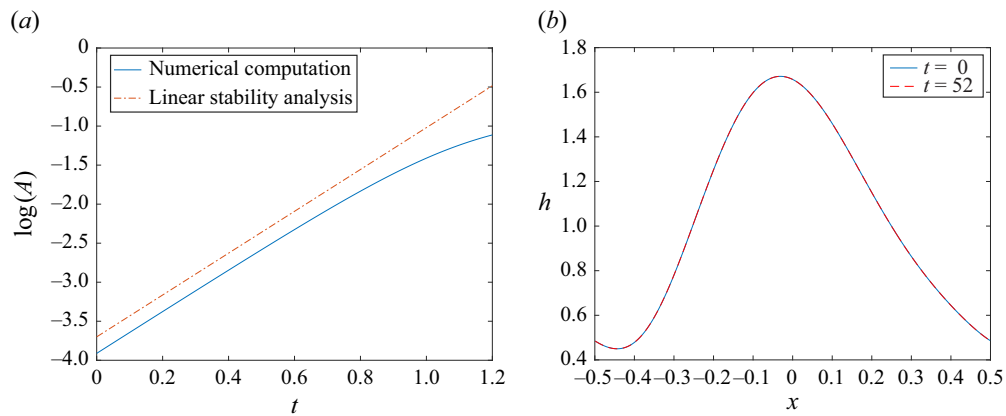
(*a*)

(*b*)

Figure 2. (*a*) Comparison of the growth rate for $d_1 = 0.8$ and $d_2 = 0.35$ and $\nu = 0.1$. Here, A is the wave amplitude. The numerical results is based on (2.33). (*b*) Comparison of transient solutions of (2.39) at $t = 0$ and $t = 40$ for $C = 23$, $D = 0.01$, $C_D = 0.1$, $R = 2.5$, $\alpha = \pi/8$ and $\delta = 0.3365$.

4. Stability and nonlinear dynamics of strong surface tension waves

4.1. *Stability of non-uniform steady states*

In Meng *et al.* (2024) we computed steady periodic wave solutions to (2.33) (equivalently (2.32)) and analysed them to develop insight into the rich bifurcation diagrams at play. Unless otherwise stated, all computations presented in this section pertain to (2.33) in order to facilitate direct comparisons with Meng *et al.* (2024). The solutions that branch off from a flat interface as infinitesimal waves (linear waves) form the primary branch, whereas solutions that bifurcate from other finite-amplitude branches are denoted as secondary branches. For primary branches, based on the values of ν obtained from weakly nonlinear analysis at the bifurcating point, we classify these further into upper and lower branches. A natural question is the stability of the steady solutions mapped out in Meng *et al.* (2024), and in cases where they are unstable the investigation of the new dynamics they get attracted to. To examine this, we choose the unimodal primary branches (upper branch in blue, lower branch in orange) computed for $d_1 = 0.8$ and $d_2 = 0.31$ in Meng *et al.* (2024), and reproduced here in figure 3(*a*). Several solutions on these two primary branches are picked and perturbed according to $h(x; t = 0) = h_0(x) + 0.1 \cos 2\pi x$, where $h_0(x)$ is the steady non-uniform periodic solution. Figure 3(*a*) also shows the location of the chosen solutions (stars for the upper branch and a diamond for the solution selected on the lower branch).

We begin with the stability of the solutions on the upper branch. The parameter q in what follows is the constant flux introduced by Meng *et al.* (2024) and arises by looking for steady solutions of (2.33) and integrating once in x. For the state corresponding to $q = 0.43$, $\nu = 0.1336$, figure 3(*b*) shows the evolution of the energy $E(t)$ of the perturbed solution indicating that it decays to a constant value corresponding to the energy of the steady solution – a comparison of $h_0(x)$ and $h(x, t = 19)$ as an inset indicates this, confirming that the solution is stable. In fact increasing the perturbation amplitudes of the initial condition to 0.2, 0.4 and 0.6 also produces the steady state we started with. The stability of another solution on the upper branch denoted as point 3 in figure 3(*a*) and corresponding to $q = 0.48$, $\nu = 0.058$, is shown in figure 3(*d*). It can be seen that the energy of the waves oscillates initially but then increase to another larger constant value (the energy of the initial steady state is depicted by the dashed line in figure 3(*d*)). This illustrates that the steady solution is unstable and the instabilities evolve into a bimodal
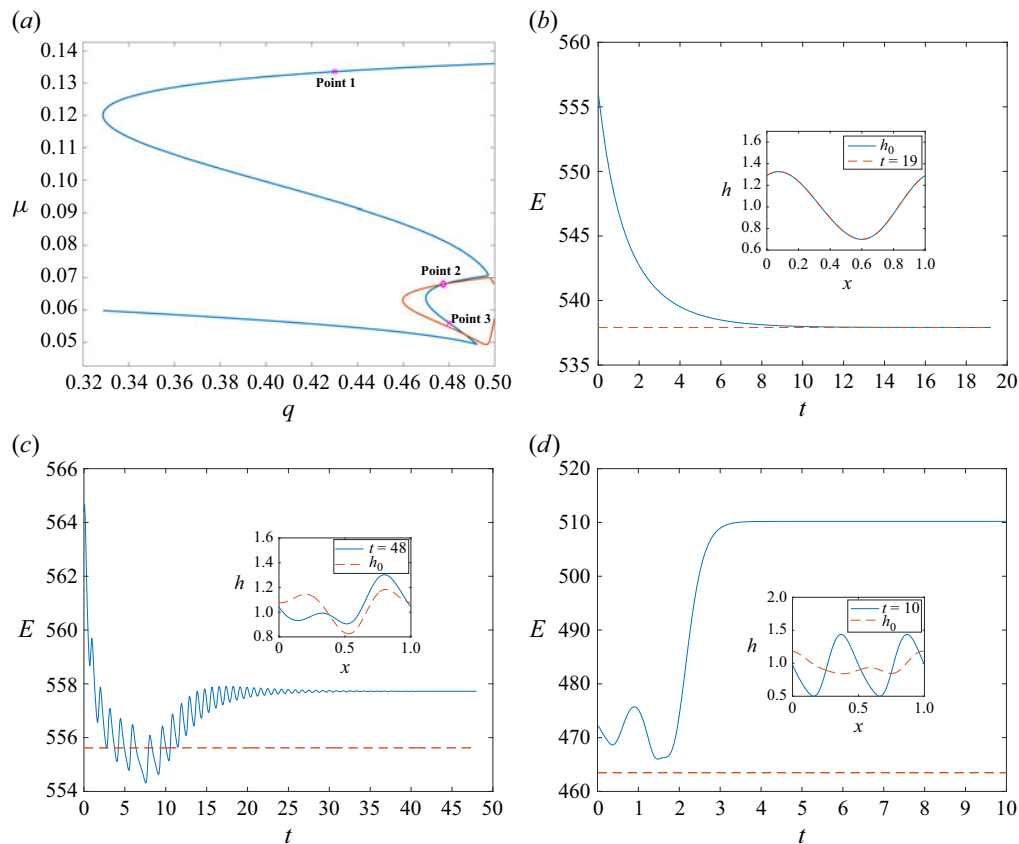
Figure 3. (*a*) The primary upper and lower branches of steady solutions of (2.33) for $d_1 = 0.8$ and $d_2 = 0.31$. The stars represent chosen solutions on upper branches, the diamond represents the chosen solution on the lower branch. (*b*–*d*) The energy and wave profiles of the perturbed solutions and the undisturbed solutions. Panel (*b*) corresponds to point 1, panel (*c*) to point 2 and (*d*) to point 3. For the energy curves, the blue solid lines represent the evolution of energy of perturbed solutions while the red dashed lines is the energy of undisturbed steady solutions.

travelling wave (see the wave profiles in the inset to figure 3(*d*) with the dashed curve denoting the initial steady state). Next, we consider the stability of the lower branch solution and in particular point 2 in figure 3(*a*) at $q = 0.4775$, $\nu = 0.068$. The results are given in figure 3(*c*) and it is seen that the energy undergoes some large amplitude oscillations before arriving to a larger constant state after a longer time. The evolution of the perturbed wave leads to the emergence of another unimodal travelling wave shown by the solid curve in the inset to figure 3(*c*); the initial steady state is depicted with a dashed curve. These representative results show that the stability of steady states is complicated. It is not easy to examine the nonlinear stability of every solution branch in the bifurcation diagrams and we do not pursue this further.

4.2. *Initial value problems, large-time dynamics and dominant attractors*

A more direct way of probing the dynamics is to solve the initial value problem subject to sinusoidal initial conditions of the form

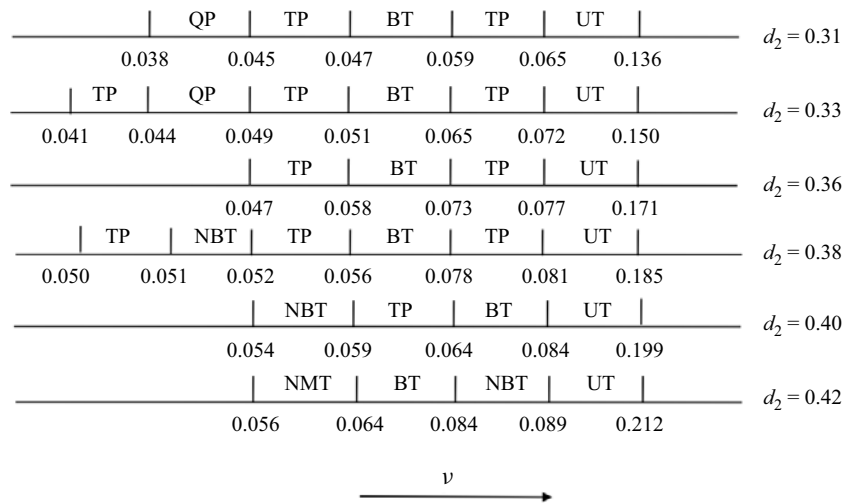$$h(x; t = 0) = 1 + 0.1[\cos(2\pi x / L) + \sin(2\pi x / L)], \tag{4.1}$$

Y. Meng, D.T. Papageorgiou and J.-M. Vanden-Broeck

| | QP | TP | BT | TP | UT | | $d_2 = 0.31$ |
| 0.038 | 0.045 | 0.047 | 0.059 | 0.065 | 0.136 | |

| TP | QP | TP | BT | TP | UT | | $d_2 = 0.33$ |
| 0.041 | 0.044 | 0.049 | 0.051 | 0.065 | 0.072 | 0.150 |

| | TP | BT | TP | UT | | $d_2 = 0.36$ |
| 0.047 | 0.058 | 0.073 | 0.077 | 0.171 | |

| TP | NBT | TP | BT | TP | UT | | $d_2 = 0.38$ |
| 0.050 | 0.051 | 0.052 | 0.056 | 0.078 | 0.081 | 0.185 |

| | NBT | TP | BT | UT | | $d_2 = 0.40$ |
| 0.054 | 0.059 | 0.064 | 0.084 | 0.199 | |

| | NMT | BT | NBT | UT | | $d_2 = 0.42$ |
| 0.056 | 0.064 | 0.084 | 0.089 | 0.212 | |

ν

Figure 4. Schematics of the various attractors for $d_1 = 0.8$. UT: unimodal travelling waves, TP: time-periodic travelling waves, BT: bimodal travelling waves, QP: quasi-periodic attractors, NBT: near-bimodal travelling waves, NMT: near-multimodal travelling waves (including near bimodal and near trimodal).

and analyse the data from a large number of numerical experiments. Different initial conditions were tested for all results presented by increasing the amplitude to values of 0.2 and adding phase shifts to the sinusoids; all reported results are attractors in the sense that they emerge for such ranges of initial conditions. In all computations that follow we choose the air-speed parameter $d_1 = 0.8$ and vary the surface tension parameter d_2. As d_2 increases surface tension becomes smaller and air-stream effects become dominant. For each fixed d_2 we carry out extensive computations to determine the dynamics and attractors as ν varies noting that as ν decreases the unscaled wave period becomes bigger. The results of these computations are presented schematically in the solution phase space in figure 4. The diagram depicts the most attracting state that emerges from the initial value problem. These have been categorised into (i) unimodal travelling waves (UT), (ii) time-periodic travelling waves (TP), (iii) bimodal travelling waves (BT), (iv) waves with quasiperiodic oscillations in time (QP), (v) near-bimodal travelling waves (NBT) and (vi) near-multimodal travelling waves (NMT). Window boundaries, where there is a transition from one state to another, have been computed within the accuracy of the reported decimals. In addition we have used the convention that the right boundary of each window represents the largest value of ν considered belonging to the window on the left. In all cases reported trivial solutions develop if ν is larger than a critical value $\nu_0(d_1, d_2)$- these are the values of rightmost windows in figure 4. In fact we can predict this by linearising (2.33) about $h = 1$ and looking for solutions of the form $\exp(2i\pi kx + st)$; setting $k = 1$ readily produces the value of ν_0 above which only trivial solutions exist

$$\nu_0(d_1, d_2) = \frac{d_2}{4\pi}\left[\frac{\pi}{d_1} + \left(\frac{\pi^2}{d_1^2} - \frac{4}{d_2}\right)^{1/2}\right]. \tag{4.2}$$

The values given by (4.2) are in complete agreement with our simulations. In addition, all solutions bifurcating from trivial states are unimodal travelling waves, as indicated in the figure. As ν decreases further the attractors depend on the surface tension parameter d_2. In what follows we describe some of these solutions to provide a quantitative picture of the dynamics.
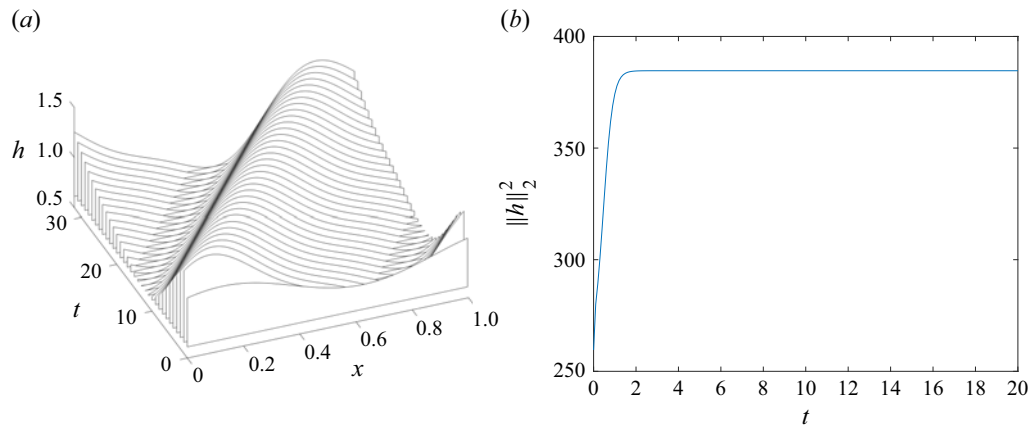
1018 A49-12

Figure 5. Unimodal travelling waves for $d_1 = 0.8$, $d_2 = 0.33$ and $\nu = 0.1$. (*a*) The evolution of the wave profile; (*b*) the evolution of the energy.

The general trends of the dynamics are depicted in the schematic of figure 4. Recall that a decrease in ν corresponds to an increase of the spatial domain size and hence an increase in the number of unstable modes entering into the nonlinear dynamics. Starting with the first window where non-trivial states are found, we see that as ν decreases, the first window of unimodal travelling waves (UT) typically gives rise to time-periodic travelling waves (TP) for the smaller values of d_2 (i.e. larger surface tension forces), or bimodal and near bimodal travelling waves for larger d_2. Further decrease in ν mostly produces bimodal travelling waves, and for the smaller values of $d_2 = 0.31, 0.33$ we observe complex dynamics that appear to be quasi-periodic in time, or time-periodic travelling waves for larger d_2.

We provide a more detailed view of the flows for the case $d_2 = 0.33$ ($d_1 = 0.8$ has been fixed also). In figures 5–8(*a*) we show representative solutions from each of the attracting windows labelled UT, TP, BT and QT in figure 4. Figure 5 has $\nu = 0.1$ and shows the evolution of the solution as it strongly gets attracted to a unimodal travelling wave – figure 5(*a*) shows the profiles as time increases and figure 5(*b*) shows the evolution of the energy, clearly indicating that all transients have disappeared for t as small as 2, approximately. It should be noted that for values of ν just larger than $\nu = 0.072$ that denotes the window boundary of the TP attractor there are very long-lived transients with oscillations that eventually decay at large times to produce a unimodal travelling wave. Figure 6 presents the solution at $\nu = 0.071$ from the time-periodic travelling wave attractor. Panel 6(*a*) shows the evolution for $t > 8.25$ to ensure that transients have disappeared as confirmed by the energy plot in panel 6(*b*) that also clearly shows the time-periodic oscillations. Decreasing ν further to 0.062 we enter the bimodal travelling wave window as seen by the results of figure 7; once again there is strong attraction to these states as seen from the evolution of the energy in panel 7(*b*) with transients gone by $t \approx 2$. A further reduction to $\nu = 0.047$ puts us in a new solution window. Here, the solution undergoes spatio-temporal oscillations that we have analysed to determine that the time oscillations are quasi-periodic. The results are provided in figure 8 which shows the spatio-temporal evolution of the interface in panel (*a*) and the corresponding energy signal that strongly indicates a complex dynamics. Further data analysis of the latter suggests that the flow is quasi-periodic (for example, we did not observe any fractal folding behaviour in Poincaré maps). It is noted that when $\nu \leqslant 0.041$ another bifurcation takes place to produce, initially at least, trimodal travelling waves. The computation can be continued by further decreasing ν
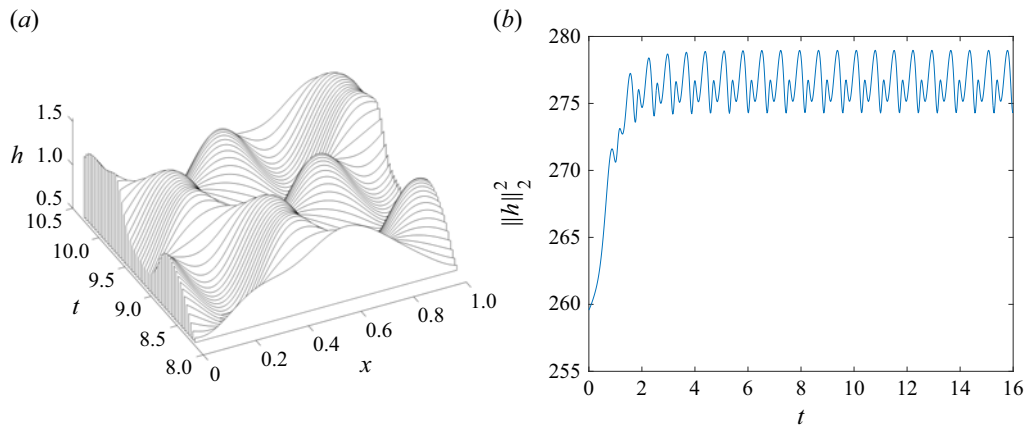
(*a*)

(*b*)

Figure 6. Time-periodic attractors for $d_1 = 0.8$, $d_2 = 0.33$ and $\nu = 0.071$. (*a*) The evolution of the wave profile; (*b*) the evolution of the energy.
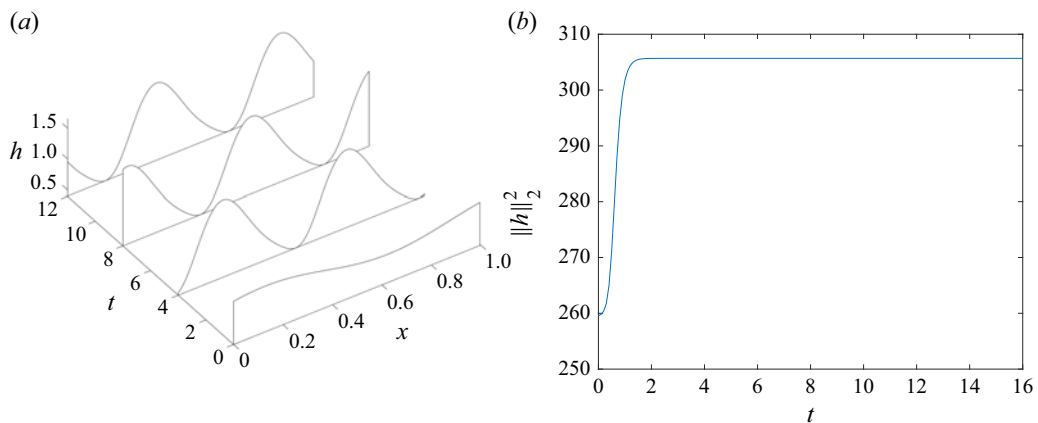
(*a*)

(*b*)

Figure 7. Bimodal travelling waves for $d_1 = 0.8$, $d_2 = 0.33$ and $\nu = 0.062$. (*a*) The evolution of the wave profile; (*b*) the evolution of the energy.

and tracking subsequent attractors but for brevity we restrict our results by obtaining the value of ν for the onset of the trimodal travelling waves. Therefore, the lowest values of ν reported in figure 5 for different d_2, correspond to the value where solutions first develop into trimodal travelling waves. It is worth noting that we can obtain qualitatively similar schematics of the various attractors when d_2 is fixed and d_1 decreases, but for brevity the results are not included here.

From figure 4, we observe that an increase of the values of d_2 leads to a qualitatively different dynamics. For example, increasing d_2 to 0.36, appears to remove the quasi-periodic solutions window found for $d_2 = 0.31$ and $d_2 = 0.33$. It is also noted that a type of near-bimodal waves first appear for $d_2 = 0.38$. When d_2 further increases to $d_2 = 0.4$, the window of time-periodic states between the unimodal and bimodal travelling waves disappears; however, there still exist time-periodic solutions between the windows of bimodal and trimodal or near-trimodal travelling waves. When $d_2 = 0.42$ and as μ is decreased, only travelling waves can be observed preceding the onset of trimodal travelling waves. Larger values of d_2 were also explored in order to establish dominant trends.
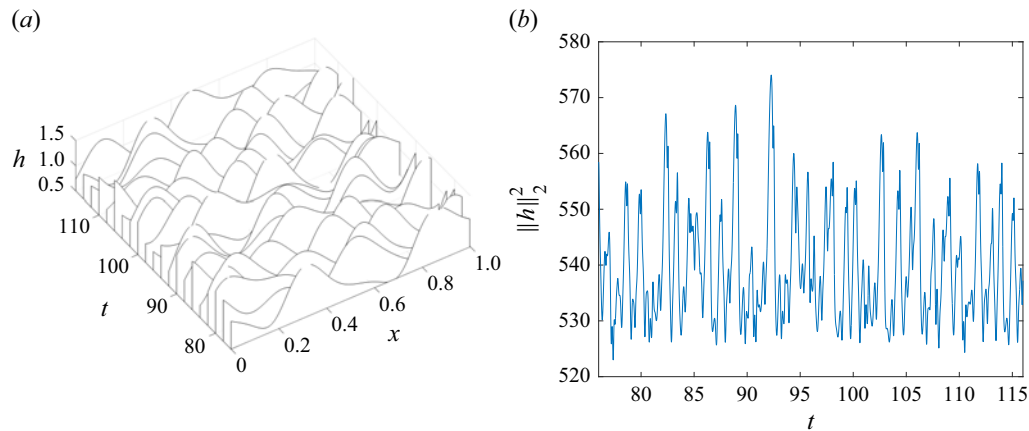
1018 A49-14

(*a*)

(*b*)

Figure 8. The quasi-periodic solution for $d_1 = 0.8$, $d_2 = 0.33$ and $\nu = 0.047$. (*a*) The evolution of the wave profile; (*b*) The evolution of energy signals.

We find that, as d_2 increases, travelling waves attain larger amplitudes and have a tendency to touch down onto the substrate. A typical result is given in figure 9(*a*) for $d_1 = 0.8$, $d_2 = 0.7$ and $\nu = 0.23$. This behaviour is also observed for the upper primary branch in Meng *et al.* (2024) when the limiting configuration of waves with fixed d_1 is considered. We note that there is a fundamental connection between the steady-state solutions of Meng *et al.* (2024) and the travelling wave solutions computed here. In King *et al.* (1993) and Meng *et al.* (2024) the film thickness is picked so as to give zero phase speeds for linear waves, and these are then followed into the nonlinear regime with the mean film thickness being part of the solution. In the present initial value problems it is more convenient to fix the mean film thickness – linear waves in general have non-zero phase speeds as expected. We expect, therefore, that the structure of the branches is similar and the numerical solutions given in figure 9(*a*) attest to this. The travelling wave solutions emerging in long-time computations are located on the upper branches if we computed the bifurcation diagrams for the travelling waves.

4.3. *Near-multimodal travelling waves*

Next we turn to the appearance of the near-bimodal travelling waves denoted by NBT in the schematic of figure 4. Figure 9(*b*) shows a typical wave profile of this type for $d_1 = 0.8$, $d_2 = 0.4$ and $\nu = 0.057$ (note that this results from the large-time evolution of the waves starting with initial condition (4.1)). The wave speed of this solution is approximately -0.6. Similar wave solutions were also found on vertical liquid films in Salamon, Armstrong & Brown (1994), where a period-doubling symmetry was used to find the secondary solutions. In order to trace the appearance of these waves, we consider the bifurcation of travelling waves having the same wave speeds in the $\nu - q$ plane, where q is the flux. More specifically, looking for travelling waves of (2.33) of the form $h(x - ct)$ and integrating once, we find

$$-\frac{c}{2h^2} + \frac{3}{2h} + \frac{\nu^2 \pi}{d_1} \mathcal{H}[h_{xx}] + \frac{\nu^3}{d_2} h_{xxx} - \nu h_x - 1 = \frac{q}{h^3}. \qquad (4.3)$$

Equation (4.3) is the same as that studied by Meng *et al.* (2024) for steady waves if we set $c = 0$ and allow the mean film thickness to emerge as part of the solution. For a more direct comparison with our time-dependent solutions we fix the mean thickness
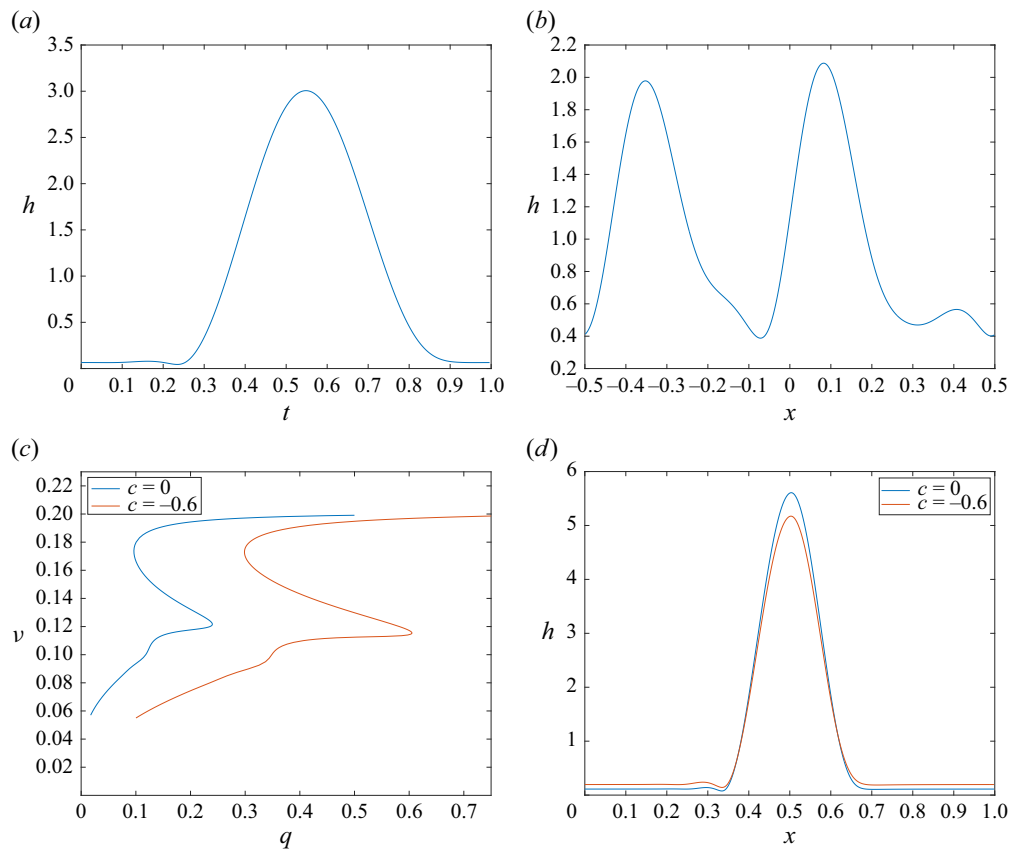
1018 A49-15

Figure 9. (*a*) The wave profile for $d_1 = 0.8$, $d_2 = 0.7$ and $v = 0.23$. (*b*) The wave profile for $d_1 = 0.8$, $d_2 = 0.4$ and $v = 0.057$. The wave speed is approximately -0.6. (*c*) The bifurcation diagrams of travelling wave solutions with fixed mean thickness of 1 for $d_1 = 0.8$, $d_2 = 0.4$. The wave speeds are -0.6 and 0. (*d*) Wave profiles for $v = 0.057$ on the bifurcation curves in figure 9(*c*).

to be 1 and compute the solutions with wave speed $c = 0$ and $c = -0.6$, by constructing $v - q$ bifurcation curves, as shown in figure 9(*c*) for the case $d_1 = 0.8$ and $d_2 = 0.4$. The bifurcation curves are similar to the steady primary upper branches in our previous study Meng *et al.* (2024), while all solutions here have mean thickness 1 as mentioned above. Since the bifurcation curves in figure 9(*c*) branch off from infinitesimal linear waves, they are denoted as primary upper branch solutions in this section. It should be noted that the bifurcation computed here are similar to the primary branch in Salamon *et al.* (1994) since the solutions in both studies start from a flat free surface. The difference is that the flux of the primary solution branch in Salamon *et al.* (1994) is fixed. We see that branches with different wave speeds have similar shapes, and the solutions corresponding to $v = 0.057$ on these branches are shown collectively in figure 9(*d*)). By comparison of the wave profiles we preclude the possibility that the near-bimodal travelling waves are located on these primary branches. However, these type of near-bimodal solutions were found in Meng *et al.* (2024) when they calculated the secondary bifurcation branches. It is reasonable to conclude, therefore, that the near-bimodal travelling waves are on the secondary bifurcation branch. This in turn implies that the unimodal, near-bimodal and bimodal travelling waves emerging in the time-dependent computations presented in this study belong to different bifurcation diagrams. Additional evidence for this follows by
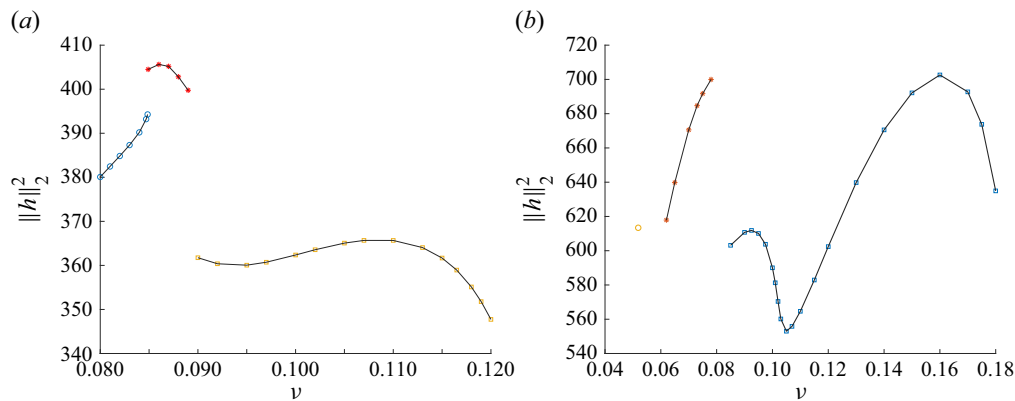
Figure 10. The variation of the energy of travelling waves for $d_1 = 0.8$ and different d_2. Panel (*a*) shows $d_2 = 0.42$. From left to right, the three branches correspond to waves of the bimodal, near-bimodal and unimodal type. Panel (*b*) shows $d_2 = 0.38$. From left to right, the three branches correspond to waves of the near-bimodal, bimodal and unimodal type.

examination of the energy of these travelling waves as ν varies, and in figure 10 we present the cases $d_1 = 0.8$, $d_2 = 0.42$ and $d_2 = 0.38$. In figure 10(*a*), the jumps in the energy show that there exist three distinct solution branches in the range $0.08 \leqslant \mu \leqslant 0.12$, corresponding to the bimodal, near-bimodal and unimodal travelling waves, respectively. We also examine the energy variation for $d_2 = 0.38$. It can be seen from figure 10(*b*), that the jump also exists for this case. For $d_2 = 0.38$, the window of the near-bimodal waves is very narrow. The energies of the solutions in this window are very close, therefore, in the plot we only include the energy of one solution (others are graphically indistinguishable). The fact that near-multimodal travelling waves appear when the value of d_2 is above a threshold reveals the change of stability of solutions on the secondary bifurcation branches as d_2 increases. When d_2 is relatively small (smaller than 0.38, roughly), the solutions on the secondary bifurcation branches are all unstable and hence travelling wave solutions of this type do not appear as large-time solutions of our time-dependent computations. The stable travelling wave solutions appear to be exclusively located on the primary bifurcation branches. As the value of d_2 increases above 0.38, some solutions on secondary bifurcation branches become stable and the near-bimodal waves (analogously for the near-trimodal waves – confirmed numerically but results not included here) appear as global attractors in the time-dependent computations.

4.4. *Bimodal, trimodal and tetramodal travelling waves*

In figure 11, we depict the boundaries for the onset of both bimodal and trimodal waves in (d_2, ν) space, for fixed $d_1 = 0.8$; as surmised from the results of the schematic (figure 4), bimodal and trimodal travelling waves appear as ν is decreased for a fixed value of d_2. The dashed (red) line in figure 11 shows the boundary of ν below which bimodal travelling waves emerge (the open circles are results from the computations and the straight line is the result of a least squares fit of the open circle data). With a decrease in ν trimodal travelling waves appear and the boundary is now depicted by the dash-dotted line (purple), with diamonds representing computations and the straight line is a least squares fit of the diamond data. Further decrease in ν produces tetramodal travelling waves as shown – the crosses come from nonlinear computations and the solid (magenta) line is derived from the bimodal curve using the symmetry scaling $\nu \to \nu/2$, see below. Interestingly, similar phenomena were also found in the weakly nonlinear dynamics of

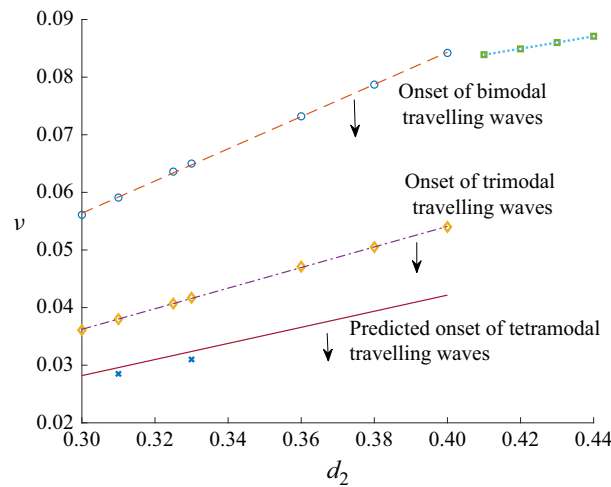Figure 11. The boundary for the onset of bimodal (the dashed red line and dotted blue line), trimodal (the dashed-dotted line) and tetramodal(the solid line) travelling wave solutions in the $d_2 - \mu$ plane for $d_1 = 0.8$. The boundary for the onset of tetramodal travelling waves is predicted by the boundary of bimodal travelling waves by the scaling $\nu \rightarrow \nu/2$. The data marked by crosses are obtained numerically.

perfectly conducting electrified falling liquid films by Tseluiko & Papageorgiou (2006), where constant slopes are found for a specific boundary between attractors despite the change of the computation domain parameter (analogous to our ν). For the fully nonlinear model studied here, the solution boundaries are more complicated. For example, the boundary of the bimodal travelling waves for $d_2 < 0.41$ has larger slope than that for $d_2 \geqslant 0.41$, which is shown in figure 11 with a dotted green line and square symbols coming from nonlinear computations. This break in the curve indicates that, for sufficiently large d_2, the onset of bimodal waves happens at a smaller ν than what would be predicted by the extrapolated linear behaviour of the range of smaller d_2 values (e.g. $d_2 \leqslant 0.41$ in this example). As seen in figure 11, there is a gap between these two boundaries in the interval $0.4 < d_2 < 0.41$. This fact is consistent with what we described above in § 4.3: the near-bimodal travelling waves on the secondary bifurcation branches change their stability and become stable when d_2 is large enough. For the values of ν in this gap, the solutions develop into the near-bimodal waves instead of the bimodal waves – this has been confirmed numerically. Comparing the bimodal and trimodal boundaries in the range $d_2 \leqslant 0.41$, we find that the values of ν on the former boundary has values of ν that are approximately 1.5 times of those on the trimodal wave boundary. As mentioned, the boundaries (the lines) for the bimodal and trimodal travelling waves are obtained by the least square fits of the numerical data (the circles, squares and diamonds). Using the scaling laws $\nu \rightarrow \nu/2$ of the boundaries, we can predict the boundary for the onset of tetramodal travelling waves from the boundary of bimodal waves by the scaling. To verify this predicted boundary, we carried out numerical computations to find the onset values of ν for two values of $d_2 = 0.31$ and $d_2 = 0.33$ (marked by crosses). Good agreement is found with the predicted boundary.

5. Dynamics of nonlinear inertio-capillary waves driven by an air stream

In this section, we focus on the effect of inertia on the spatio-temporal characteristics of air-blown waves governed by (2.39). The equation is solved on spatially periodic domains of period L; most results consider unit periods and for comparison purposes

we also present some runs with period 2π. It is useful to consider the linear stability properties of (2.39) around the uniform flat state $h = 1$. Looking for solutions of the form $\exp(2\pi i k x/L + st)$, where the integer k is the wavenumber of the disturbances, implies that the growth rate s_r where $s = s_r + i s_i$ is

$$\frac{1}{\delta} s_r = \frac{2\bar{C}}{3} \beta^3 |k| k^2 - \frac{1}{3\bar{D}} \beta^4 k^4 + \left(\frac{8R}{15} - \frac{4R\bar{\tau}}{15} - \frac{2}{3} \cot \alpha \right) \beta^2 k^2, \qquad \beta = \frac{2\pi}{L}. \quad (5.1)$$

Note that, in the absence of the air stream, i.e. $\bar{C} = \bar{\tau} = 0$, instability of flat states is possible only if $R > R_c = 5 \cot \alpha /4$. This is typically the case studied by numerous authors – see for example Pumir, Manneville & Pomeau (1983), Rosenau, Oron & Hyman (1992), Oron & Gottlieb (2002) and Scheid *et al.* (2005). To evaluate the effect of the air stream in our model, we consider $R < R_c$, so that in the absence of the air we would expect perturbations to die out at large times.

5.1. *Low Reynolds numbers: time-periodic attractors and nonlinear travelling waves*

We begin with the case $\delta = 0.03$ and carry out numerical computations on periodic domains of unit length ($\beta = 2\pi$ in (5.1)), with $\bar{C} = 0.69$, $\bar{D} = 13.33$, $\bar{\tau} = 1.84$ and $\alpha = \pi/8$. The range of Reynolds numbers in this numerical experiment is $0 < R \leqslant 0.7$. Note that even for the largest Reynolds number $R = 0.7$, we have $8R/15 - 2 \cot \alpha /3 \approx -1.24$ placing us firmly in the subcritical stable regime in the absence of an outer air flow. Using the chosen parameters in (5.1) we find that, for all $0 < R \leqslant 0.7$, there are two linearly unstable modes, $k = 1$ and $k = 2$. The evolution becomes highly nonlinear even on such relatively short domains due to the energy supplied by the air stream to rapidly increase the wave amplitude via an interaction with the inertial terms – we provide quantitative details later. Our computations show that in the range $0.5 \leqslant R \leqslant 0.7$ the solutions develop into nonlinear travelling waves, while at smaller R in the range $0 < R < 0.5$, no travelling waves appear and the solutions saturate to time-periodic attractors with different temporal oscillation periods. Figure 12(*a*) and figure 12(*b*) show the variation of wave speed and amplitudes of the travelling waves in the range $0.5 \leqslant R \leqslant 0.7$. It can be seen that with the increase of the Reynolds number, the wave speeds and amplitudes increase, a feature that was also found in falling liquid film flows without the air stream, see Pumir *et al.* (1983). In fact, when we further increase R slightly to 0.73, the solutions become unbounded (discussed in detail later). Details of the time-periodic solutions found for $0 < R < 0.5$ are given in figure 12(*c*) which plots the time period T of the oscillations against R. It is seen that as R increases the time period decreases monotonically at an apparently linear rate until the attractor looses stability to travelling waves at $R \geqslant 0.5$.

5.2. *Reynolds number above critical: blow up in finite time*

Now we turn to the phenomenon of unbounded solutions of the Benney equation documented in the absence of an air stream when the Reynolds number exceeds a critical value. Such singular behaviour of the Benney equation was first reported numerically by Pumir *et al.* (1983). The stability structure, including both bounded and unbounded solutions, was later investigated by Rosenau *et al.* (1992) and Oron & Gottlieb (2002) described the phenomenon quantitatively by numerically calculating the boundary between the regions of bounded and unbounded solutions in (ϵ, R) space, where ϵ is equivalent to our slenderness parameter δ. In later work Scheid *et al.* (2005) connected dynamical systems theory to the numerical results obtained by Oron & Gottlieb (2002). They concluded that the absence of one-hump travelling wave solutions is related to the finite-time blow up of the Benney equations. Note that the results mentioned above are
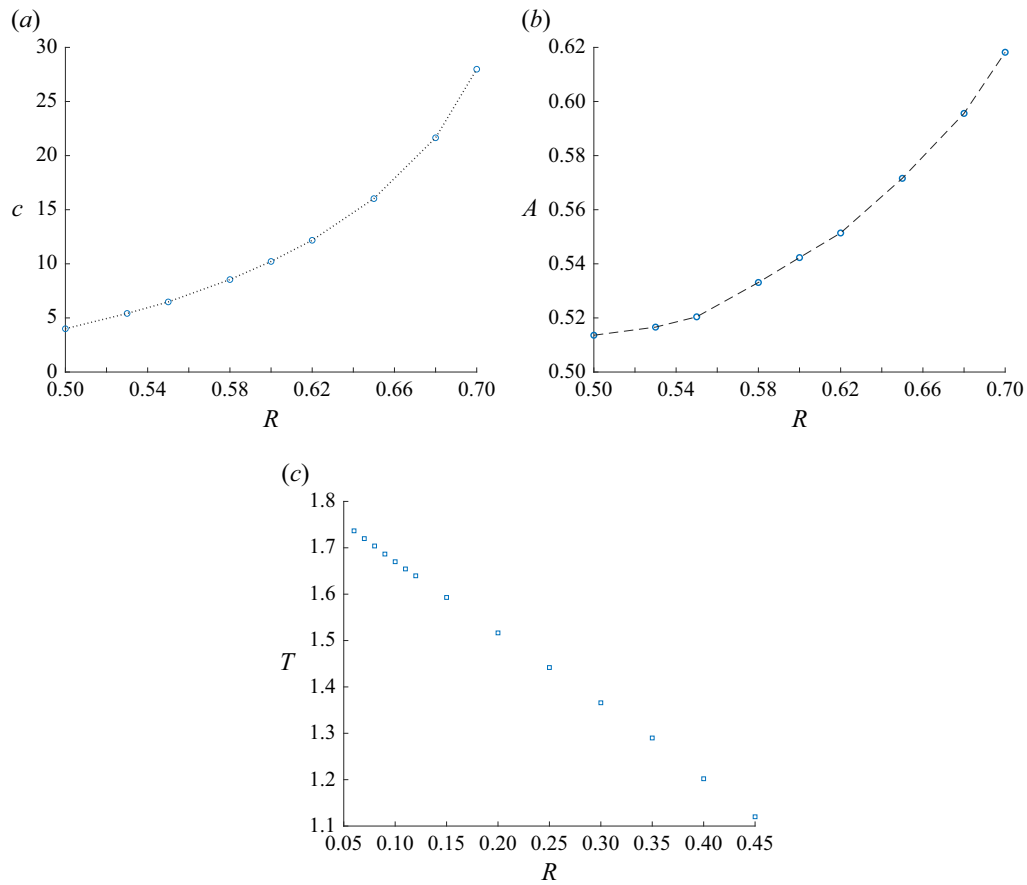
(a)

(b)

(c)

Figure 12. Effect of the Reynolds number on (a) travelling wave speeds, (b) travelling wave amplitudes and (c) periods of oscillations of time-periodic solutions, for $\bar{C} = 0.69$, $\bar{\tau} = 1.84$, $\bar{D} = 13.33$, $\alpha = \pi/8$ and $\delta = 0.03$.

based on the classical Benney equation with the instability arising from the h_{xx} term when $R > 5 \cot \alpha / 4$. For the present counter-current air/liquid problem, the presence of the air stream enhances the instabilities and leads to rich phenomena when we consider the boundary between the bounded and unbounded solution regions in parameter space.

We have carried out extensive numerical computations to categorise the dynamics and different attractors in the $R - \delta$ parameter plane, in order to evaluate the novel effects of the air stream on subcritical unforced Benney solutions. All computations having $\bar{C} = \bar{\tau} = 0$ would be stable. The way we construct this solution space is to fix the unscaled air-stream parameter C and surface tension parameter D and study the effect of varying δ. To fix matters we considered $C = 23$, $C_D = 0.08$, $D = 0.012$ and $\alpha = \pi/8$. In terms of these unscaled parameters (recall from § 2.2 that $\bar{C} = \delta C$, $\bar{D} = D/\delta^2$ and $\bar{\tau} = CC_D = \mathcal{O}(1)$) (2.39) reads

$$h_t + \left[-\frac{2}{3}h^3 + \frac{CC_D}{2}h^2 + \delta \left(\frac{8R}{15}h^6 - \frac{4RCC_D}{15}h^5 - \frac{2\cot\alpha}{3}h^3 \right) h_x \right.$$
$$\left. + \frac{2\delta^2 C}{3}h^3 \mathcal{H}[h_{xx}] + \frac{\delta^3}{3D}h^3 h_{xxx} \right]_x = 0. \tag{5.2}$$
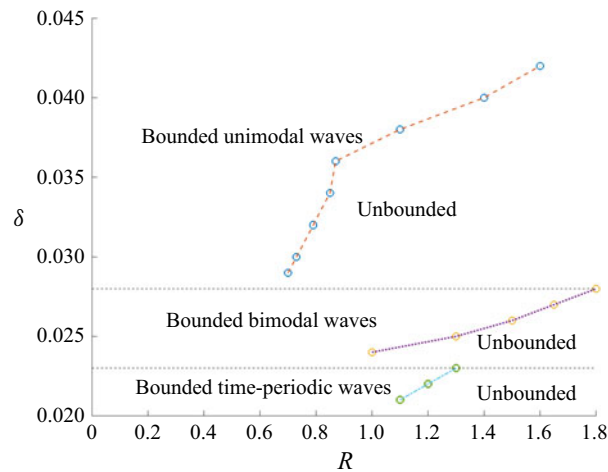
Figure 13. The boundary between the domains of bounded and unbounded solutions for the Benney equation computed numerically for $C = 23$, $C_D = 0.08$, $D = 0.012$, $\alpha = \pi/8$.

The spatial period is set to $L = 1$ and the initial value problem of (5.2) is computed as R and δ are varied. This is more convenient than working with the scaled (2.39) which requires $\overline{C}$ and $\overline{D}$ to change according to the scalings given above every time δ is changed. The results are presented collectively in figure 13. For every value of the slenderness parameter δ, there exists a critical value of the Reynolds number below which the solutions are bounded at large times and above it a finite-time blow up is found. Below this critical value the dynamics of the bounded solutions is rich and depends on the value of δ. Figure 13 identifies three regions, delineated by the horizontal dashed lines. For δ between 0.02 and 0.023 we find bounded solutions to the left of the dashed-green curve that are time-periodic travelling waves. When δ is approximately between 0.024 and 0.028 the bounded solutions to the left of the purple-dashed curve now evolve to give bimodal travelling waves, and for δ larger than approximately 0.029 and 0.043 we obtain bounded unimodal travelling waves to the left of the red-dashed curve. It is interesting to note that, in Oron & Gottlieb (2002), the boundaries in the $R - \delta$ plane are given for what they term $n = 1$ and $n = 2$ solutions that represent the one-hump and two-hump travelling waves. As outlined above the situation is different here and bounded attractors below critical values of R are more complicated and analogous to those for the inertialess solutions presented in figure 4 in § 4.2.

Some typical results showing blow up are depicted in figures 14(*a*) and 14(*b*). The parameters for this run are $\delta = 0.0232$ and $R = 2$. We are slightly above the critical Reynolds boundary and two unstable modes are present according to the dispersion relation (5.1) with $L = 1$ the growth rate curve is shown in the upper part of figure 14(*d*) with the two unstable modes $k = 1$ and $k = 2$ indicated by a circle. Figure 14(*a*) superposes the interfacial profiles at three different times just before blow up – the times are given in the inset to figure 14(*a*). A narrowing of the wave profiles can be observed coupled with a rapid growth in the wave amplitude. In the adjacent panel 14(*b*) we show the spatial behaviour of the three competing nonlinear terms in (2.39) at the final computed time $t = 9.7867$ just prior to the blow up. to better understand the singularity. The spatial dependence of the inertial term, surface tension term and air-induced pressure term at $t = 9.7867$ are plotted in figure 14(*b*). These terms are the surface tension term shown in blue, the inertial term shown in red and the air-induced pressure term shown in orange.
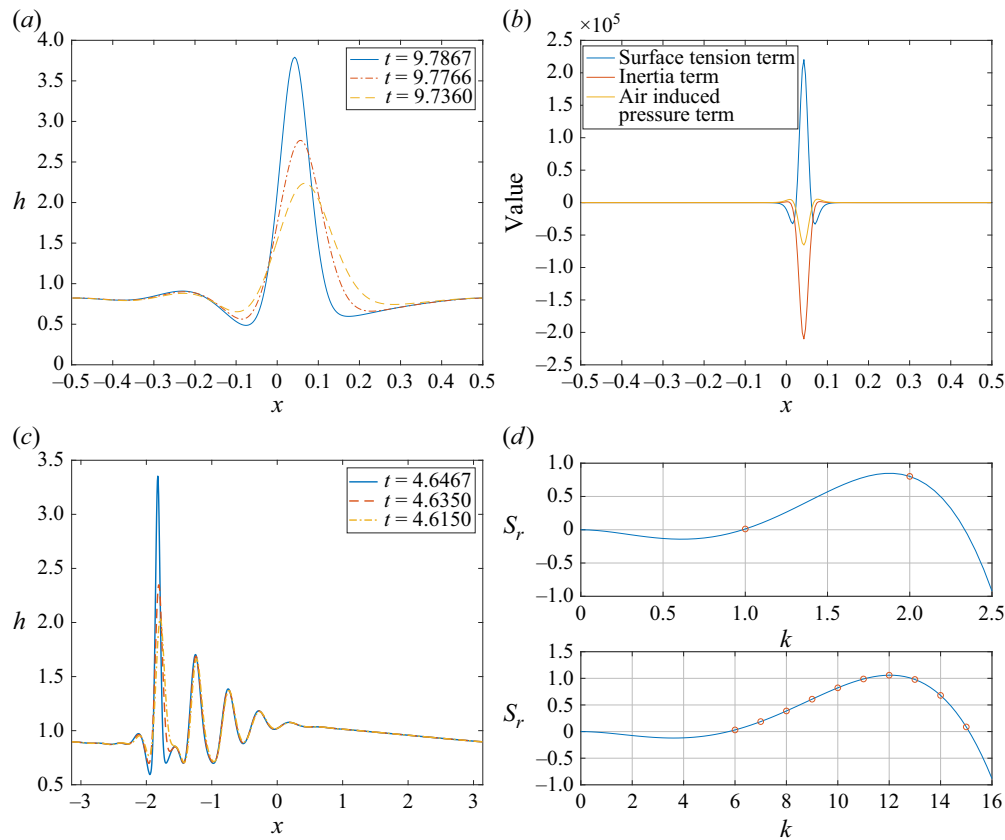
Figure 14. (*a*) The shape of the surface at three different times with the parameters $C = 22$, $D = 0.011$, $\delta = 0.0232$, $C_D = 0.08$, $\alpha = \pi/8$ and $R = 2$ just preceding the blow-up. The computation domain $L = 1$. (*b*) The size of different terms at $t = 9.7867$. (*c*) The shape of the surface at three different times with the parameters $C = 22$, $D = 0.011$, $\delta = 0.0232$, $C_D = 0.08$, $\alpha = \pi/8$ and $R = 3$ just preceding the blow-up. The computation domain $L = 2\pi$. (*d*) Growth rate for $L = 1$ (above) and $L = 2\pi$ (below) for the two cases discussed here. The wavenumbers with positive growth rate are marked by circles.

The data indicate that there is a dominant balance between surface tension and inertia, with the air-induced pressure being asymptotically subdominant. The role of the air stream is to induce instability and drive the system into a highly nonlinear regime that produces a balance between surface tension and inertia. It is expected, therefore, that the singular structure will be the same as for the Benney equation as described by Pumir *et al.* (1983). If the singularity takes place at $t = t_s$ and at position $x = x_s$, then the self-similar solution near the singularity is

$$h \sim (t_s - t)^{-1/9} G(\xi), \qquad \xi = \frac{x_s - x}{(t_s - t)^{1/6}}, \qquad (5.3)$$

where the shape function G satisfies a nonlinear ordinary differential equation in $-\infty < \xi < \infty$. We do not pursue this analysis further here since it has been addressed for the Benney problem, however, we have confirmed that scalings in (5.3) are consistent with our numerical data. We have also carried out computations on larger domains that support more linearly unstable modes. A blow up singularity is encountered once again, but with additional nonlinear wavy structures in the final profile. The case $L = 2\pi$ is included in figure 14(*c*) that shows the solution at three consecutive times close to the singularity.
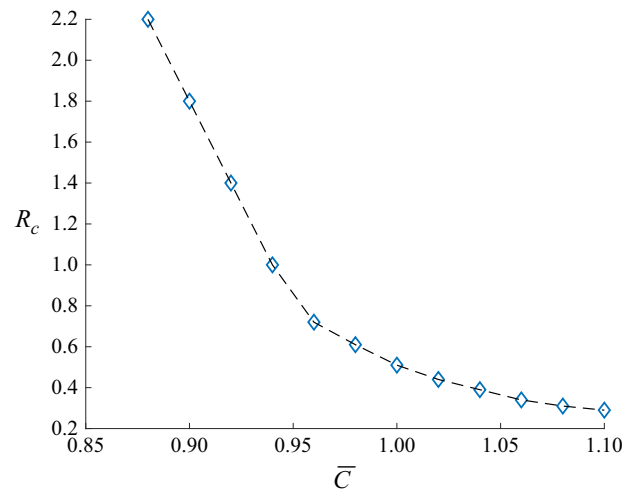
Figure 15. The effect of the scaled air-stream parameter $\overline{C}$ on the critical value R_c of the Reynolds number where the transition from bounded to unbounded solutions occurs. Here, $\delta = 0.04$, $C_D = 0.08$ ($\overline{\tau} = CC_D = \overline{C}C_D/\delta = 2\overline{C}$), $\overline{D} = 7.5$ ($D = 0.012$), $\alpha = \pi/8$. Diamonds represent computational data.

The wave structures arise due to the additional unstable modes (there are now 10 unstable modes) as shown in the lower panel of figure 14(*d*). Note that both growth rate curves in figure 14(*d*) are of Turing type and support short-wave unstable modes due to the presence of the air stream. These new modes are exclusively due to the air stream since in its absence the flow would be stable. In addition, instabilities without the air stream are only possible above a critical Reynolds number and are of the long-wave type.

In the last part of this section, we explore the effect of the air stream $\overline{C}$ on the critical value of R that heralds a transition from bounded to unbounded solutions. We do this for a fixed value $\delta = 0.04$, a fixed value of $D = 0.012$ (equivalently $\overline{D} = 7.5$), $\alpha = \pi/8$, and also fix $C_D = 0.08$, i.e. $\overline{\tau} = CC_D = 2\overline{C}$, given the scaling $C = \overline{C}/\delta$. Hence, we can study the blow up behaviour in terms of the two parameters $\overline{C}$ and R. Solution of the initial value problem allowed us to numerically estimate the boundary between bounded and unbounded solutions in the $(\overline{C}, R_c)$ space, where R_c is our estimate for the critical Reynolds number. The results are given in figure 15. It can be seen that the presence of the air stream enhances singularity formation of the air-stream Benney equation in the sense that blow up occurs at smaller values of the Reynolds number as the air speed increases. The decrease in R_c is monotonic and quite strong – an increase of $\overline{C}$ from approximately 0.9 to 1.1, causes a tenfold decrease in R_c from 2.2 to 0.2. These results suggest that the air stream can be used systematically to trigger large amplitude waves in the flow in the system.

5.3. *Effects of non-uniform shear stress*

In this section the effects of non-uniform tangential stress that can be introduced by the air stream are investigated for both the surface tension dominated and the inertio-capillary regimes. Tseluiko & Kalliadasis (2011) treated the interface as a rigid wall, to leading order, and modelled the tangential and normal stresses induced by a counter-flowing turbulent gas. The analytical results were also compared with the experiments of Thorsness, Morrisroe & Hanratty (1978) that measured the spatial variation of shear stress by the turbulent flow along a solid wall with small sinusoidal indentations. The theory shows good agreement with the experiments. In light of their results, we now discuss the effect of the variation of the tangential stress on the models developed here under

the assumption of a constant shear stress. Our main aim is to evaluate the effect of non-uniform shear derived from theoretical and experimental studies, on the nonlinear terminal dynamics of the inertio-capillary regime.

Following Tseluiko & Kalliadasis (2011), the tangential shear can be represented by the order-one constant term (τ_{w0}) and higher-order variations ($\tau_{w1} \cdots$). The surface tension dominated model (2.32) arises at leading order and only order-one terms are retained, i.e. τ_{w0}. The non-uniform shear stress has no effect on the surface tension dominated regime. For the inertio-capillary regime, the higher-order variation τ_{w1} will enter into the next-order equation in the formulation. It is straightforward to modify our derivation to include this term. The modified equation reads

$$h_t + \left[-\frac{2}{3}h^3 + \frac{\overline{\tau}}{2}h^2 + \delta \left(\frac{8R}{15}h^6 - \frac{4R\overline{\tau}}{15}h^5 - \frac{2\cot\alpha}{3}h^3 \right) h_x + \frac{2\delta\overline{C}}{3}h^3 \mathcal{H}[h_{xx}] \right.$$

$$\left. + \frac{\delta}{3\overline{D}}h^3 h_{xxx} + \delta\frac{\overline{\tau}}{2}\tau_{w1}[h]h^2 \right]_x = 0, \quad (5.4)$$

where $\tau_{w1}[h]$ is a linear non-local operator involving h and has been calculated by Tseluiko & Kalliadasis (2011) (its symbol $\widehat{\tau_{w1}}(k)$ say, in Fourier space is known). From the dispersion relation (figure 12 in Tseluiko & Kalliadasis (2011)), it can be seen that the inclusion of this term introduces instabilities and alters the linear wave speed. It should be noted that, in their paper, the positive x direction is opposite to that in the present paper, implying that for our coordinate system the real part of $\widehat{\tau_{w1}}(k)$ is positive. We expect therefore, that for sufficiently low Reynolds numbers (i.e. prior to any blow-up events), it is more likely that the nonlinear waves travel upwards. We do not pursue travelling waves further and concentrate more on blow-up events.

We now focus on the blow-up behaviour of solutions to (5.4) incorporating spatial variations depending on the interfacial position in the tangential shear stress. We examine the cases with parameters $C = 23$, $D = 0.012$, $\alpha = \pi/8$ and $C_d = 0.08$ (the same parameters as in figure 13). Two values of δ are chosen, $\delta = 0.038$ and $\delta = 0.042$. The initial conditions are the same as those used in figure 13. For the constant tangential stress, the critical Reynolds numbers above which blow-up occurs for these two values of δ are approximately 1.1 and 1.6, respectively. Solution of (5.4) incorporating shear-stress variations are given in figure 16. The figure shows the energy evolution of solutions corresponding to $\delta = 0.038$ (*a*) and $\delta = 0.042$ (*b*), for different Reynolds numbers. It is strongly suggested that the critical Reynolds numbers where the solutions go unbounded do not change noticeably, indicating that inclusion of the next-order variation of shear stress has little effect on the blow-up boundary. Note that, if we do not assume that the air speed is large enough to induce the modulated pressure term, the equation obtained reduces to the model in Tseluiko & Kalliadasis (2011). In such a regime, the unstable modes introduced by the air into the system arise from the variation of shear stress alone (the mean part of the shear stress contributes an advective term linearly). It is expected that the critical Reynolds numbers where solutions go unbounded will change, but the self-similar solutions near the singular time remain same and produce a balance between surface tension and inertia. For the solutions with low Reynolds numbers, the inclusion of the non-uniform shear stress potentially alters the speed of nonlinear travelling waves.

6. Conclusions

In this paper, we have investigated the dynamics of a thin liquid film flowing down an inclined wall in the presence of an upward flowing air stream parallel to the wall. In the
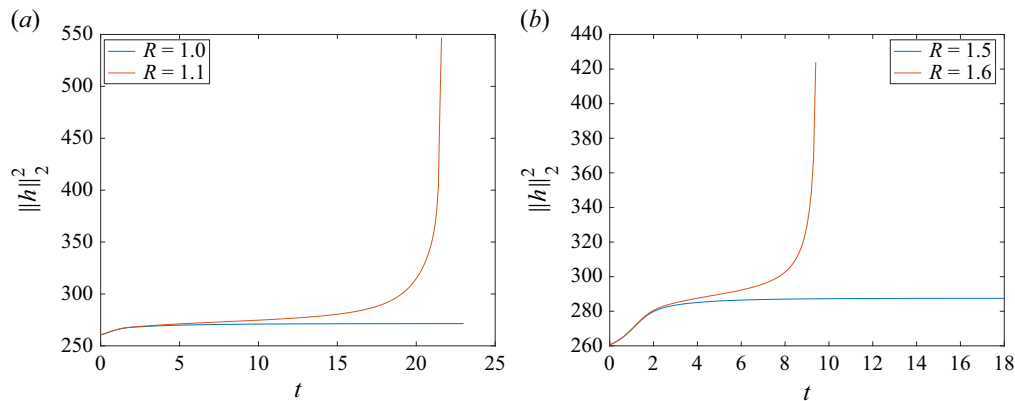
Figure 16. The energy evolution of transient solutions of different values of δ: (*a*) $\delta = 0.038$; (*b*) $\delta = 0.042$.

modelling of this gas–liquid system, we consider the gas and liquid problems separately and make some assumptions to make analytical progress in deriving a reduced-dimension nonlinear evolution equation to study the problem in detail. In the incompressible gas region we introduce the velocity potential governed by the two-dimensional Laplace equation. Under the assumption of small gas–liquid interfacial amplitudes (small relative to the outer gas region but of the same order as the mean liquid film thickness), the pressure induced by the air stream on the liquid film is obtained analytically. The interfacial tangential stress induced by the air stream is taken to be constant, an empirical assumption that is supported by experimental observations – see Tu & Wood (1996), Mendez *et al.* (2021). With the outer flow supplying a forcing on the interface, we subsequently focus on the problem of a thin liquid film and derive model equations describing the dynamics of the interface under different dominant balances including inertialess and inertial models of the air-stream Benney equations. Steady solutions of the inertialess model have been studied in detail by Meng *et al.* (2024), who give a fairly complete picture of the bifurcations. The stability of solutions and subsequent evolution to different attractors was not considered and the present work undertakes this task, among others.

A large number of numerical experiments are carried out centring around these two long-wave models in order to elucidate the rich dynamics of the air-blown waves on the interface of viscous liquid film flows. For the numerical computation, we adopt the second-order implicit–explicit BDF scheme for time marching combined with a Newton iteration due to the nonlinear nature of the systems. To accelerate the computation at every time step, spectral matrices are used to build analytically the Jacobian matrix required in the Newton iteration. The accuracy of this numerical method is confirmed by comparing the growth rates given by the numerical computation and closed form linear stability results.

For the inertialess model, a typical picture of the various types of solution attractors is constructed as the air speed and surface tension parameters are varied – these are the parameters d_1 and d_2 in (2.33). We varied d_2 for fixed $d_1 = 0.8$, and also confirmed (not included here for brevity) that the behaviour at different d_1 is qualitatively similar – bigger d_1 requires bigger d_2 to produce analogous solution windows like the ones given in figure 4. The wave profiles and energy signals of typical solution types are shown, including unimodal and bimodal travelling waves, time-periodic travelling wave attractors and temporally quasi-periodic solutions. It is found that, as d_2 increases (surface tension decreases), the schematics of the attractors are qualitatively different. This is distinct from the results of the weakly nonlinear version of the

equation as discussed in Tseluiko & Papageorgiou (2006) for the electrified falling film problem. It is interesting to note that, when d_2 is above a certain value, a new type of travelling wave solutions, denoted as near-bimodal waves, appear. To track the origin for the appearance of this type of wave, we examine in detail the case $d_1 = 0.8$ and $d_2 = 0.4$ and compute travelling wave bifurcations for fixed mean film thicknesses (typically equal to 1 in dimensionless terms). The results show that the near-bimodal travelling waves are not located on the primary bifurcation branches. This is also confirmed by the disjointed branches of the energy variation of travelling waves with the inverse wavelength parameter ν; there are jumps in the energy as ν varies and we transition from uni-modal, near-bimodal and bimodal travelling waves for the typical case $d_1 = 0.8$ and $d_2 = 0.42$. It is speculated, therefore, that the multi-modal travelling waves are solutions on the secondary bifurcation. The increase of d_2 changes the stability of solutions on the secondary bifurcation: below a critical value of d_2, travelling wave solutions on the secondary bifurcation branch are unstable whilst some of these solutions become stable above a critical value.

The effect of an outer air stream on inertio-capillary waves was also considered. This regime, developed in § 2.2 and Appendix A, derives from weaker surface tension, namely the capillary number is of order δ^2 rather than order δ^3 that leads to the strong surface tension regime derived in § 2.1. Inertia, surface tension and air-stream effects enter order δ nonlinear regularising terms and lead to (2.39). Comparison of (2.39) with the strong surface (2.32) shows that the former has high nonlinearities (e.g. $h^6 h_{xx}$ inertial terms) in addition to the possibility of instabilities arising at sufficiently large values of R – see the dispersion relation (5.1) for example. It is also established that the induced pressure on the interface due to the air stream introduces linear instabilities that dominate those due to inertia (if present) in the short-wave limit. We concentrated on flows with sufficiently small R that would be stable in the absence of the air stream (linearly this condition is $R < 5 \cot \alpha / 4$) and computed the effect of increasing the air-stream speed through the parameter $\overline{C}$ (or C). For fixed δ we find that as the Reynolds number increases from zero the flow dynamics evolves to give time-periodic travelling waves or nonlinear travelling waves at larger values of R. In all cases we find that a further increase of the Reynolds number results in finite-time singularities that have the same structure as those for the Benney equation in the absence of the air stream. It is also observed that blow up occurs as the Reynolds number increases above some critical value for every δ. The boundaries between the regions of bounded and unbounded solutions as well as the type of solutions in the subcritical regime are calculated numerically for a wide range of δ and R. We also calculated the effect of the air stream on the critical Reynolds number R_c above which blow up occurs, other parameters held fixed. We find that R_c monotonically decreases with the scaled air-stream speed $\overline{C}$, decreasing by a factor of 10 for the range of $\overline{C}$ considered as seen in figure 15. Physically, our results suggest that large amplitude wave structures heralded by the singular solutions found for small R and sufficiently large dimensionless air speed C, could be possible routes to the fragmentation and atomisation of the liquid layer.

In addition, the effects of non-uniform tangential stress on the models developed in this paper are investigated by including non-uniform stresses arising from an outer turbulent gas flow. We do this by following the asymptotic solutions and models derived in Tseluiko & Kalliadasis (2011), where it is shown that the tangential stress is constant to leading order and spatial variations (depending on the interfacial shape in a non-local manner) enter at the next order in the slenderness parameter. It follows, therefore, that the higher-order variation of shear stress does not appear in the surface tension dominated model (2.39) which emerges directly at leading order and which supports intricate nonlinear solutions. For the inertio-capillary regime, the variation of shear stress

leads to a non-local nonlinear term included at first order, which introduces additional instability and potentially alters wave speeds – see (5.4). This new equation is solved numerically in order to evaluate the effects of non-uniform shear on the blow-up behaviour of solutions. Typical cases show that the inclusion of the higher-order variation has little effect on the blow-up boundary and the structure of the singular solutions which arise from a balance between nonlinear inertia terms and surface tension terms. When blow-up occurs the models break down since the wave amplitude will have the same order of magnitude as the wavelength. Physically, we would expect fragmentation and droplet formation, phenomena that in general must be addressed with direct numerical simulations.

Declaration of interests. The authors report no conflict of interest.

Appendix A. The inertio-capillary evolution equation

Recall the asymptotic expansions in § 2.2 and the leading-order solutions (2.36), (2.37)

$$u_0 = y(y - 2h_0) + \overline{\tau}y, \quad v_0 = h_{0x}y^2, \quad \frac{1}{2}R\overline{p}_0(x,t) = h_0 \cot\alpha - \overline{C}\mathcal{H}[h_{0x}] - \frac{1}{2\overline{D}}h_{0xx},$$

(A1)

and the associated leading-order evolution equation (2.38). The momentum and continuity equations at first order become

$$u_{0t} + u_0 u_{0x} + v_0 u_{0y} + \overline{p}_{0x} = \frac{1}{R}u_{1yy}, \quad p_{1y} = v_{0yy}, \quad u_{1x} + v_{1y} = 0,$$

(A2)

and are subject to the boundary conditions

$$u_1 = v_1 = 0 \quad \text{at } y = 0,$$

(A3)

$$v_{0y}|_{h_0} h_1 + v_1|_{h_0} = h_{1t} + u_0|_{h_0} h_{1x} + u_{0y}|_{h_0} h_{0x} h_1 + u_1|_{h_0} h_{0x},$$

(A4)

$$u_{1y}|_{h_0} = 0.$$

(A5)

Note that the second of (A2) is not needed in the analysis at first order but is included for completeness. Using solutions (2.36) in (A4), simplifies the latter to

$$h_{1t} + \overline{\tau}(h_0 h_1)_x - \left(h_0^2 h_1\right)_x + u_1|_{h_0} h_{0x} - v_1|_{h_0} = 0,$$

(A6)

which, on use of the continuity equation to write $v_1|_{h_0} = -\int_0^{h_0} u_{1x}\mathrm{d}y$, casts (A6) into

$$h_{1t} + \overline{\tau}(h_0 h_1)_x - \left(h_0^2 h_1\right)_x + \partial_x\left(\int_0^{h_0} u_1 \mathrm{d}y\right) = 0.$$

(A7)

Our task is to express (A6) in terms of h_0 and h_1. Integration of (A2) and use of (A3) and (A5) gives

$$u_1 = R\left[\left(-\frac{1}{3}y^3 + yh_0^2\right)h_{0t} + \frac{1}{3}y\left(\frac{1}{2}y^3 - 2h_0^3\right)h_0 h_{0x} + \frac{\overline{\tau}}{3}y\left(-\frac{1}{4}y^3 + h_0^3\right)h_{0x}\right]$$
$$+ R\left(\frac{1}{2}y^2 - yh_0\right)\overline{p}_{0x}.$$

(A8)

Substitution of (A8) into (A7), and using (2.38) to eliminate h_{0t} in favour of $x-$derivatives, gives the following equation for h_1:

$$h_{1t} + \overline{\tau}(h_0 h_1)_x - \left(h_0^2 h_1\right)_x + R\left(\frac{8}{15}h_0^6 h_{0x} - \frac{4}{15}\overline{\tau}h_0^5 h_{0x} - \frac{1}{3}h_0^3 \overline{p}_{0x}\right)_x = 0. \qquad (A9)$$

A regularised equation for $h := h_0 + \delta h_1$ (that ignores terms of $\mathcal{O}(\delta^2)$ or smaller) is found by adding (2.38) to δ times (A9), namely

$$h_t + \left(\frac{\overline{\tau}}{2}h_0^2 + \delta\overline{\tau}h_0 h_1 - \frac{2}{3}h_0^3 - \delta h_0^2 h_1\right)_x + \delta R\left(\frac{8}{15}h^6 h_x - \frac{4}{15}\overline{\tau}h^5 h_x - \frac{1}{3}h^3 \overline{p}_{0x}\right)_x = 0, \qquad (A10)$$

where it is understood that the dependence of $\overline{p}_0$ is now on h rather than h_0 (the penalty for this is $\mathcal{O}(\delta^2)$ which is consistent with our two-term approximation). The second term under the $x-$derivative can be written as

$$\frac{\overline{\tau}}{2}\left(h_0^2 + 2\delta h_0 h_1\right) - \frac{2}{3}\left(h_0^3 + 3\delta h_0^2 h_1\right) = \frac{\overline{\tau}}{2}h^2 - \frac{2}{3}h^3 + \mathcal{O}(\delta^2), \qquad (A11)$$

and this produces the desired evolution (2.32)

$$h_t + \frac{\partial}{\partial x}\left[\frac{\overline{\tau}}{2}h^2 - \frac{2}{3}h^3 + \frac{8}{15}\delta R h^6 h_x - \frac{4}{15}\delta R\overline{\tau}h^5 h_x\right.$$
$$\left. - \frac{\delta}{3}h^3\left(2h_x\cot\alpha - 2\overline{C}\mathcal{H}[h_{xx}] - \frac{1}{\overline{D}}h_{xxx}\right)\right] = 0. \qquad (A12)$$

REFERENCES

AKRIVIS, G., PAPAGEORGIOU, D.T. & SMYRLIS, Y.-S. 2011 Linearly implicit methods for a semilinear parabolic system arising in two-phase flows. *IMA J. Numer. Anal.* **31**, 299–321.

ALEKSEENKO, S.V., AKTERSHEV, S.P., CHERDANTSEV, A.V., KHARLAMOV, S.M. & MARKOVICH, D.M. 2009 Primary instabilities of liquid film flow sheared by turbulent gas stream. *Intl J. Multiphase Flow* **35**, 617–627.

CAMASSA, R., OGROSKY, H.R. & OLANDER, J. 2017 Viscous film-flow coating the interior of a vertical tube. Part 2. Air-driven flow. *J. Fluid Mech.* **825**, 1056–1090.

CHANG, H.-C. 1986 Nonlinear waves on liquid film surfaces—I. Flooding in a vertical tube. *Chem. Engng Sci.* **41**, 2463–2476.

DEMEKHIN, E.A. 1981 Nonlinear waves in a liquid film entrained by a turbulent gas stream. *Fluid Dyn.* **16**, 188–193.

FRANK, A.M. 2008 Numerical simulation of gas driven waves in a liquid film. *Phys. Fluids* **20** (12), 122102.

HANRATTY, T.J. & ENGEN, J.M. 1957 Interaction between a turbulent air stream and a moving water surface. *AIChE J.* **3**, 299–304.

HANRATTY, T.J. & HERSHMAN, A. 1961 Initiation of roll waves. *AIChE J.* **7**, 488–497.

ISHIMURA, M., MERGUI, S., RUYER-QUIL, C. & DIETZE, G.F. 2023 Gas-sheared falling liquid films beyond the absolute instability limit. *J. Fluid Mech.* **971**, A37.

JEFFREYS, H. 1925 LXXXIV. *The flow of water in an inclined channel of rectangular section. Lond. Edinburgh Dublin Phil. Mag. J. Sci.* **49** (293), 364–373.

KING, A.C., TUCK, E.O. & VANDEN-BROECK, J.-M. 1993 Air-blown waves on thin viscous sheets. *Phys. Fluids* **5**, 973–978.

KOFMAN, N., MERGUI, S. & RUYER-QUIL, C. 2017 Characteristics of solitary waves on a falling liquid film sheared by a turbulent counter-current gas flow. *Intl J. Multiphase Flow* **95**, 22–34.

LAVALLE, G., GRENIER, N., MERGUI, S. & DIETZE, G.F. 2020 Solitary waves on superconfined falling liquid films. *Phys. Rev. Fluids* **5**, 032001.

MCCREADY, M.J. & CHANG, H.-C. 1996 Formation of large disturbances on sheared and falling liquid films. *Chem. Engng Commun.* **141-142**, 347–358.

MENDEZ, M., GOSSET, A., SCHEID, B., BALABANE, M. & BUCHLIN, J.-M. 2021 Dynamics of the jet wiping process via integral models. *J. Fluid Mech.* **911**, A47.

MENG, Y., PAPAGEORGIOU, D.T. & VANDEN-BROECK, J.-M. 2024 Steady wind-generated gravity-capillary waves on viscous liquid film flows. *SIAM J. Appl. Maths* **84**, 477–496.

MIESEN, R. & BOERSMA, B.J. 1995 Hydrodynamic stability of a sheared liquid film. *J. Fluid Mech.* **301**, 175–202.

ORON, A. & GOTTLIEB, O. 2002 Nonlinear dynamics of temporally excited falling liquid films. *Phys. Fluids* **14**, 2622–2636.

ÖZGEN, S., CARBONARO, M. & SARMA, G.S.R. 2002 Experimental study of wave characteristics on a thin layer of de/anti-icing fluid. *Phys. Fluids* **14** (10), 3391–3402.

PENG, C.A., JURMAN, L.A. & MCCREADY, M.J. 1991 Formation of solitary waves on gas-sheared liquid layers. *Intl J. Multiphase Flow* **17**, 767–782.

PUMIR, A., MANNEVILLE, P. & POMEAU, Y. 1983 Bounded and unbounded patterns of the benney equation. *J. Fluid Mech.* **135**, 27–50.

ROSENAU, P., ORON, A. & HYMAN, J.M. 1992 Bounded and unbounded patterns of the Benney equation. *Phys. Fluids* **4**, 1102–1104.

RUYER-QUIL, C. & MANNEVILLE, P. 2000 Improved modeling of flows down inclined planes. *Eur. Phys. J. B* **15** (2), 357–369.

SALAMON T.R., ARMSTRONG R.C. & BROWN R.A. 1994 Traveling waves on vertical films: numerical analysis using the finite element method. *Phys. Fluids* **6**, 2202–2220.

SCHEID, B., RUYER-QUIL, C., THIELE, U., KABOV, O.A., LEGROS, J.C. & COLINET, P. 2005 Validity domain of the Benney equation including the Marangoni effect for closed and open flows. *J. Fluid Mech.* **527**, 303–335.

SEMYONOV, P.A. 1944 Flows of thin liquid films. *J. Tech. Phys.* **14**, 427–437.

SMITH, F.R.P. 1970 Stability of liquid film flow down an inclined plane with oblique air flow. *Phys. Fluids* **13**, 1693–1700.

SMYRLIS, Y.-S. & PAPAGEORGIOU, D.T. 1991 Predicting chaos for infinite dimensional dynamical systems: the Kuramoto-Sivashinsky equation, a case study.. *Proc. Natl Acad. Sci. USA* **88**, 11129–11132.

THORSNESS, C.B., MORRISROE, P.E. & HANRATTY, T.J. 1978 A comparison of linear theory with measurements of the variation of shear stress along a solid wave. *Chem. Engng Sci.* **33**, 579–592.

TREFETHEN, L.N. 2000 *Spectral methods in MATLAB*. SIAM.

TRIFONOV, Y.Y. 2010*a* Flooding in two-phase counter-current flows: numerical investigation of the gas–liquid wavy interface using the Navier–Stokes equations. *Intl J. Multiphase Flow* **36**, 549–557.

TRIFONOV, Y.Y. 2010*b* Counter-current gas-liquid wavy film flow between the vertical plates analyzed using the Navier–Stokes equations. *AIChE J.* **56**, 1975–1987.

TRIFONOV, Y.Y. 2011 Counter-current gas-liquid flow between vertical corrugated plates. *Chem. Engng Sci.* **66**, 4851–4866.

TSELUIKO, D. & KALLIADASIS, S. 2011 Nonlinear waves in counter-current gas–liquid film flow. *J. Fluid Mech.* **673**, 19–59.

TSELUIKO, D. & PAPAGEORGIOU, D.T. 2006 Wave evolution on electrified falling films. *J. Fluid Mech.* **556**, 361–386.

TSVELODUB, O.Y. & BACHAROV, A.A. 2018 Simulating solitary waves on a flowing down liquid film entrained by a gas stream. *Eur. J. Mech. - B/Fluids* **72**, 449–455.

TSVELODUB, O.Y. & BACHAROV, A.A. 2020 Studying the topological structure of steady-state travelling solutions for the model of film flow of a viscous fluid entrained by a gas flow. *Eur. J. Mech. - B/Fluids* **81**, 15–22.

TU, C. & WOOD, D. 1996 Wall pressure and shear stress measurements beneath an impinging jet. *Expl Therm. Fluid Sci.* **13**, 364–373.

TUCK, E.O. 1975 On air flow over free surfaces of stationary water. *J. Austral. Math. Soc.* **19** (Series B), 66–80.